

# Development drives dynamics of living chiral crystals

Tzer Han Tan<sup>1,2,5</sup>, Alexander Mietke<sup>3,5</sup>, Hugh Higinbotham<sup>4,6</sup>, Junang Li<sup>4,6</sup>, Yuchao Chen<sup>4</sup>, Peter J. Foster<sup>4</sup>, Shreyas Gokhale<sup>4</sup>, Jörn Dunkel<sup>3</sup>, Nikta Fakhri<sup>4,7</sup>

<sup>1</sup> Quantitative Biology Initiative, Harvard University, Cambridge, MA, USA

<sup>2</sup> Center for Systems Biology Dresden, Dresden, Germany

<sup>3</sup> Department of Mathematics, Massachusetts Institute of Technology, Cambridge, MA, USA

<sup>4</sup> Department of Physics, Massachusetts Institute of Technology, Cambridge, MA, USA

<sup>5</sup> These authors contributed equally and are joint first authors.

<sup>6</sup> These authors contributed equally.

<sup>7</sup> Corresponding author: fakhri@mit.edu

## Abstract

Active crystals are highly ordered structures that emerge from the nonequilibrium self-organization of motile objects, and have been widely studied in synthetic [29, 9] and bacterial [31, 30] active matter. Whether collective crystallization phenomena can occur naturally in groups of autonomously developing multicellular organisms is currently unknown. Here, we show that swimming starfish embryos spontaneously assemble into chiral crystals that span thousands of spinning organisms and persist for tens of hours. Combining experiment, hydrodynamic theory, and simulations, we demonstrate that the formation, dynamics, and dissolution of these living crystals are controlled by the natural development of the embryos. Remarkably, the living chiral crystals exhibit self-sustained oscillations with dynamic signatures recently predicted to appear in odd elastic materials [36]. More generally, our work demonstrates how autonomous morphological development at the single-organism level can control emergent collective nonequilibrium dynamics and symmetry breaking at the macroscale.

## Main text

Symmetry breaking [1, 2] is a hallmark of living [25] and synthetic [29, 10, 18, 23] active matter. From the asymmetric growth of multicellular organisms [25, 27, 39] to the coherent motions of swimming cells [34, 40] and self-propelled colloids [29, 10, 38, 6], active systems form self-organized structures [21, 43] with unusual material properties [3, 41, 4] that can only emerge far from thermal equilibrium. In spite of major experimental [29, 10, 31, 40, 41, 6] and theoretical [26, 37, 11] progress over the last decade, we are only beginning to understand how complex collective behaviors of multicellular [7, 19, 32, 12] and multiorganismal [35, 8] systems arise from the broken symmetries and nonequilibrium dynamics of their individual constituents.

A particularly interesting class of nonequilibrium symmetry-breaking phenomena comprises the active crystallization processes recently discovered in colloidal [29] and bacterial [31] systems. Unlike conventional passive crystals, which form upon lowering temperature and often require attractive forces, active crystallization arises from the particles' self-propulsion and can occur even in purely repulsive dilute systems [29]. A long-standing related, unanswered question is whether groups of multicellular organisms can self-organize into states of crystalline order and, if so, what emergent material properties they might exhibit.

Here, we report the discovery of spontaneous crystallization in large assemblies of developing starfish *Patiria miniata* embryos (Fig. 1a). Our experimental observations show how, over the course of their natural development, thousands of swimming embryos come together to form living chiral crystal (LCC) structures that persist for many hours. In contrast to externally actuated colloidal systems, the self-assembly, dynamics, and dissolution of these LCCs are controlled entirely by the embryos' internal developmental program (Fig. 1a,b). A quantitative theoretical analysis reveals that LCC formation arises from the complex hydrodynamic interactions [14, 22] between the starfish embryos. Once formed, these LCCs exhibit striking collective dynamics, consistent with predictions from a recently proposed theory of odd elasticity [36].

### **Self-assembly, growth, and dissolution of starfish embryo crystals**

During early development, starfish embryos experience substantial morphological changes. From the onset of gastrulation (Fig. 1b, 0 h), an embryo elongates along its anterior-posterior (AP) axis (0–44 h) while progressively developing folds that further break shape symmetry. In parallel, the topology of the self-generated fluid flows near the embryo's surface changes substantially (Fig. 1b), reflecting spatial reconfiguration of the cilia during growth [16], similar to what has been reported in other ciliated organisms [42]. Remarkably, when embryos swim toward the water-air interface, they can attain a stable configuration such that their AP axes align perpendicular to the interface. Groups of embryos aligned in this manner can spontaneously self-organize into two-dimensional hexagonal clusters (Fig. 1a, 2–5 h). Over time, these clusters grow into larger crystals, reaching sizes of hundreds to thousands of embryos (Fig. 1a, 26 h) and persisting for tens of hours. As embryos become more elongated and their flow fields become less ordered (Fig. 1b, 38–44 h), the crystals begin to disassemble (Fig. 1a, 35 h) and eventually dissolve completely (Fig. 1a, 38 h).

When viewed from above, both small and large crystals tend to rotate clockwise (Fig. 1c,d), due to the chiral (left-handed) spinning motions of individual embryos about their AP axis. Large LCCs typically exhibit a high degree of hexagonal order, while also harboring lattice defects (Fig. 1d). Misaligned embryos can act as defects with 7-fold coordination (Fig. 1d, cyan), whereas missing or departing embryos can lead to 5-fold coordinated vacancy defects (Fig. 1d, red). Both the assembly and rotational dynamics of the LCCs can be quantitatively explained by a hydrodynamic model that accounts for the flow fields generated by individual embryos (Figs. 1e and 2b).

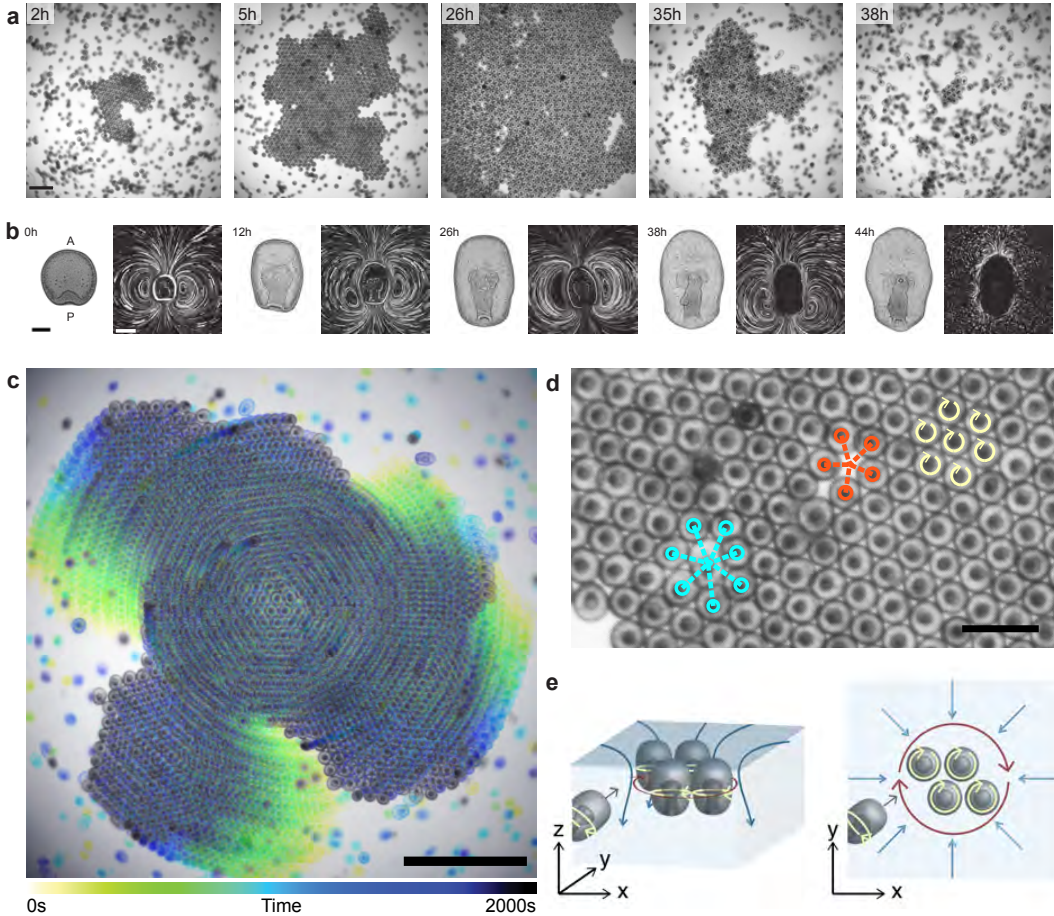


**Figure 1: Developing starfish embryos self-organize into living chiral crystals.** **a**, Time sequence of still images showing crystal assembly and dissolution. Scale bar, 1 mm.  $t = 0$  hours corresponds to the onset of clustering. **b**, Embryo morphology and flow fields change with developmental time. Shape scale bar, 100  $\mu$ m. Flow field scale bar, 200  $\mu$ m. **c**, Embryos assembled in a crystal perform a global collective rotation. Scale bar, 2 mm. **d**, Spinning embryos (yellow arrows) in the crystal form a hexagonal lattice, containing 5-fold (red) and 7-fold (cyan) defects. Scale bar, 0.5 mm. **e**, Schematic of embryo dynamics and fluid flows. Crystals of spinning embryos form near the air-water interface. Self-generated hydrodynamic flows lead to an effective attraction between surface-bound embryos.

## Hydrodynamic interactions facilitate the crystal formation and collective dynamics

To understand the hydrodynamic interactions underlying the formation and rotation of ordered clusters, we first analyzed the fluid flow around individual embryos that spin upright near the air-water interface (Fig. 2a). Observed along the AP axis in the horizontal  $xy$ -plane, fluid moves radially inward towards the embryo, reaches maximum speed 0.1–0.2 mm lateral to the embryo surface (Fig. 2b), and eventually moves toward the bottom of the well (Fig. 1e, left). The radial in-flow generated by the isolated embryos is accurately captured by a Stokeslet (blue curve in Fig. 2b), a solution to the Stokes equation that describes the generic fluid flow around a force exerting object (SI Sec. 2.1.1). The cilia-driven fluid flow compensates the gravitational force [13] acting on the negatively buoyant embryo, so that it can maintain a fixed position below the surface. Indeed, the buoyant weight force  $F_g = 1.7 \pm 0.3$  nN determined from the sedimentation speeds of immobilized embryos (SI Sec. 1.3), is of the same order as the Stokeslet strength  $F_{st} = 2.6 \pm 0.3$  nN obtained by fitting the radial in-flow data in Fig. 1b.

The self-generated Stokeslet flow stabilizes the upright AP-axis orientation of embryos (SI Sec. 2.1.2). In addition, it induces an effective long-ranged hydrodynamic attraction between embryos, facilitating the assembly of long-lived clusters at the water-air interface. Similar effects have been observed previously for bacterial and algal microswimmers near rigid surfaces [31, 14]. Once two embryos are close together, their intrinsic spinning motions lead to an additional exchange of hydrodynamic forces and torques (Fig. 2c). Similar to pairs of *Volvox* colonies near a rigid surface [14, 20], nearby starfish embryos ‘dance’ around each other, and their spinning frequency decreases compared to that of a freely spinning embryo. The excess cilia-generated torque from slower rotating embryos manifests itself in systematic azimuthal flow contributions (Fig. 2d, top). To confirm our understanding of the hydrodynamic interactions, we complemented the Stokeslet flow of each embryo with additional contributions that reflect the corresponding exchange of forces and torques in bound pairs and triplets (SI Sec. 3.2.2, Fig. S3). Flow fields fitted via this approach are in quantitative agreement with our experimental measurements (Fig. 2d, bottom).

Based on these insights, we experimentally constrained a minimal model in which upright spinning embryos are represented by rigid disks interacting through hydrodynamic Stokeslet-mediated pairwise attraction, pairwise transverse force exchange, and pairwise chiral torque exchange (SI Sec. 2.2.1). Using the Stokeslet strength determined from fits as in Fig. 2b, and a parameterization of force and torque exchanges based on rotation frequency measurements of bound pairs and triplets (SI Sec. 2.2.2), this minimal model predicts the self-organized formation of rotating clusters similar to those seen in the experiments (Fig. 2e). Moreover, the model captures the reduction of individual embryo spinning frequencies in both small and large clusters (Fig. 2f), as well as the variation of the emergent cluster rotation frequency with cluster size over several orders of magnitude (Fig. 2g).

## Increase and decrease of crystalline order with embryonic development

A striking feature of the LCCs is that they nucleate, grow and dissolve naturally as embryos progress through their development (Fig. 1a). Crystalline order increases during the growth phase, whereas the dissolution is preceded by a loss of orientational, translational, and dynamic order. To quantify the orientational order, we calculated the local bond orientational order parameter  $\psi_6(\mathbf{r}_i) = |\psi_6|_i e^{i\phi_i}$ , where  $\mathbf{r}_i$  is the position of an embryo in the co-rotating frame (SI Secs. 3.1 and 3.4). The magnitude  $|\psi_6|_i$  quantifies the local hexagonal order, and the phase angle  $\phi_i$  indicates the local bond orientation [28]. During the initial stages of self-assembly, small clusters merge together along different crystal axes, resulting in grain boundaries and broad distributions of  $|\psi_6|_i$  and  $\phi_i$  (Fig. 3a-d, (i)). However, within 5 hours of crystal formation the crystal undergoes rapid internal restructuring due to relative rotation between subdomains. This results

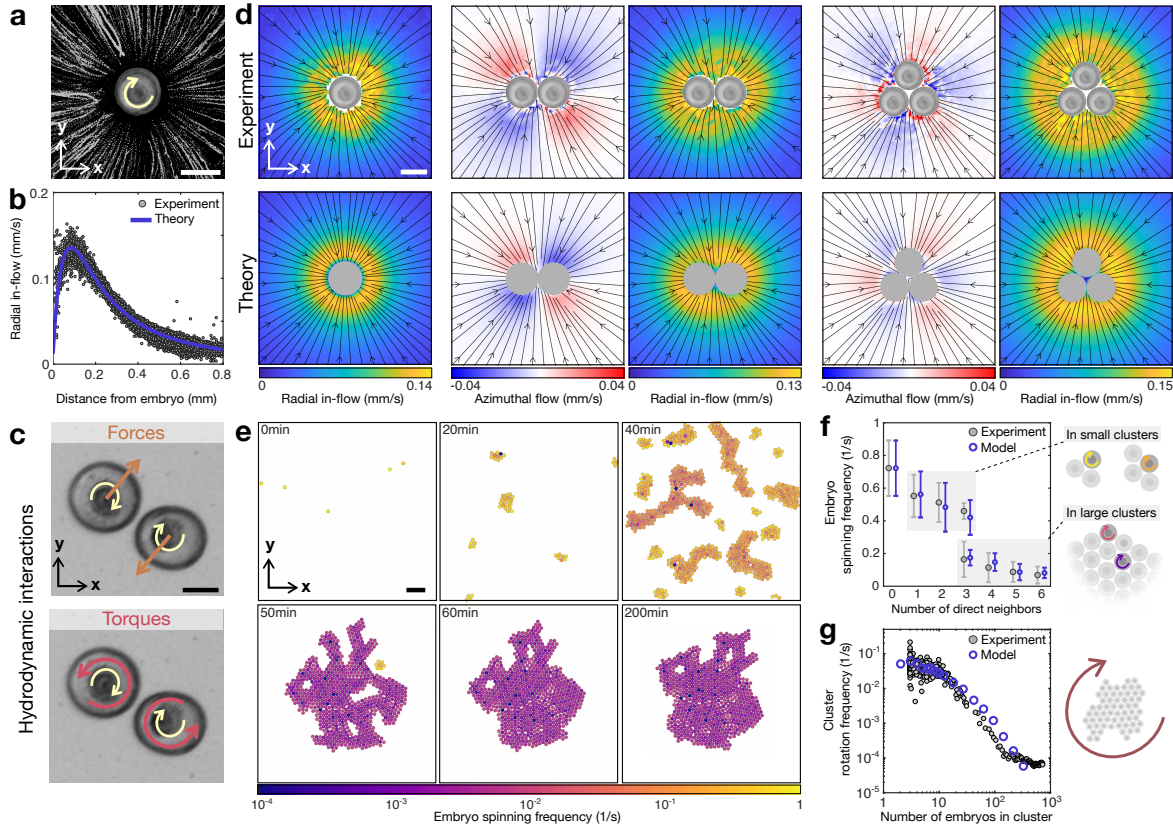


**Figure 2: Hydrodynamics facilitates crystal nucleation, growth and rotational dynamics.** **a**, Top view of a single embryo. Yellow arrow indicates spinning direction and gray dotted lines visualize streamlines through maximum projections of fluid tracer particles (SI Sec. 1.2). Scale bar,  $200\text{ }\mu\text{m}$ . **b**, Measured radial in-flow velocities (gray dots) are well-described by Stokeslet flow below a free surface (blue line) (SI Sec. 2.1.1). **c**, Spinning embryos exchange forces (brown arrows) and torques (red arrows) due to hydrodynamic interactions. As a result, nearby embryos rotate around each other while slowing-down their individual spinning frequencies. Scale bar,  $100\text{ }\mu\text{m}$ . **d**, Measured flow fields surrounding rotating pairs and triplets (top row, SI Sec. 3.2.1) can be quantitatively described with suitable solutions of the Stokes equation (bottom row, SI Sec. 3.2.2) that account for the hydrodynamic interactions in **c**. Scale bar,  $200\text{ }\mu\text{m}$ . **e**, An experimentally constrained minimal model (SI Sec. 2.2), based on Stokeslet-mediated attraction (**a,b**) and hydrodynamic near-field interactions of spinning particles (**c**), reproduces crystal formation and rotation dynamics seen in the experiments. Scale bar,  $2\text{ mm}$ . **f**, The model quantitatively predicts single embryo spinning frequencies in both small clusters ( $\leq 4$  embryos) and larger clusters ( $\sim 100$  embryos). Error bars denote standard deviations of measurements (Experiment) and from simulations (Model) (SI Sec. 2.2.3). **g**, This model also reproduces the size-dependent cluster rotation frequencies over several orders of magnitudes. Standard deviations of simulation results are smaller than symbol size.

in a large, nearly defect-free crystal with a high degree of hexagonal order ( $\langle|\psi_6|_i\rangle \approx 0.9$ ) and a narrow distribution of local bond orientation (Fig. 3a-d, (ii-iii)). This macroscopically ordered state persists for several hours.

As embryonic development progresses, changes in morphology and surrounding flow fields (Fig. 1b) eventually begin to decrease the crystalline order. This loss of order is reflected in the time evolution of measured order parameter histograms (Fig. 3b,c). As the crystal slowly loses orientational order, the probability density of  $|\psi_6|_i$  spreads to smaller values (Fig. 3b,  $t > 15$  hours), accompanied by a drift of the mean phase angle that indicates a dynamic restructuring of the crystal (Fig. 3c,  $t > 15$  hours). After about 30 hours, disorder begins to dominate and the crystal slowly dissolves over a period of 10 hours (Fig. 3a-d, (iv-v)).

To understand in more detail the evolution of crystalline order prior to dissolution, we quantified the translational order of the crystal by calculating the radial pair distribution function  $g(r)$  (Fig. 3f, inset, SI Sec. 3.5). The width of the first peak of  $g(r)$  was found to increase with development (Fig. 3f), suggesting that changes in the developing embryos lead to increased variation in the distance between nearest neighbors. As a result, deviations of embryo position from the ideal hexagonal lattice become frequent, reducing translational order.

To examine whether the progressive loss of orientational and translational order is also reflected in dynamic properties of the embryo crystal lattice, we determined the dynamic Lindemann parameter (SI Sec. 3.6). This parameter measures relative displacements between nearest neighbors in a lattice as a function of time [44]. We observe that in the crystalline phase, the Lindemann parameter increases systematically with developmental time (Fig. 3g), which indicates a progressive destabilization of the crystal lattice, consistent with the observed loss of orientational (Fig. 3e) and translational (Fig. 3f) order. The large fluctuations of the dynamic Lindemann parameter at early and late times are due to the small size and highly dynamic nature of growing and dissolving clusters.

Taken together, the systematic decay of orientational, translational and dynamic order with developmental time shows how morphological changes at the single-embryo level (Fig. 1b) can autonomously drive LCCs through a dissolution transition reminiscent of solid-gas phase transitions.

### **Emergence of chiral displacement waves and signatures of odd elasticity**

Starfish embryos are inherently chiral, as they spin about their AP axis in a left-handed manner (Fig. 1d,e). When self-organized into a cluster, a fraction of each embryo's torque is transferred to the whole crystal, resulting in a global cluster rotation (Fig. 1c). Perhaps more importantly, the chiral spinning motions also lead to transverse interactions and torque exchanges between embryo pairs (Fig. 2c). The non-reciprocal nature of these interactions raises the interesting question of whether LCCs can support self-sustained chiral waves and shear cycles, similar to those recently predicted in odd elastic materials [36].

To explore this question, we measured the displacement fields  $\mathbf{u}(\mathbf{r}_i, t) = (u_x, u_y)$  by tracking embryo positions  $\mathbf{r}_i$  in a frame co-rotating with the underlying crystal (Fig. 4a, SI Sec. 3.7). In crystals that contained a large number of vacancy defects, we observe the propagation of self-excited displacement waves which in some cases persist for longer than an hour (Fig. 4b-c). Since the dynamics of the fluid-embedded crystal lattices is overdamped, the existence of such waves is a direct manifestation of the crystal's nonequilibrium state. To establish the chiral character of the waves, we first quantified their reflection symmetry by using a mode chirality metric (SI Sec. 3.8). This analysis reveals that, during periods of active wave propagation, the dominant modes are indeed chiral (Fig. S6). In particular, the frequency of the dominant modes,  $0.28 \text{ min}^{-1}$ , is close to the spinning frequency of individual embryos within the cluster ( $0.33 \text{ min}^{-1}$ , see SI Sec. 3.3),

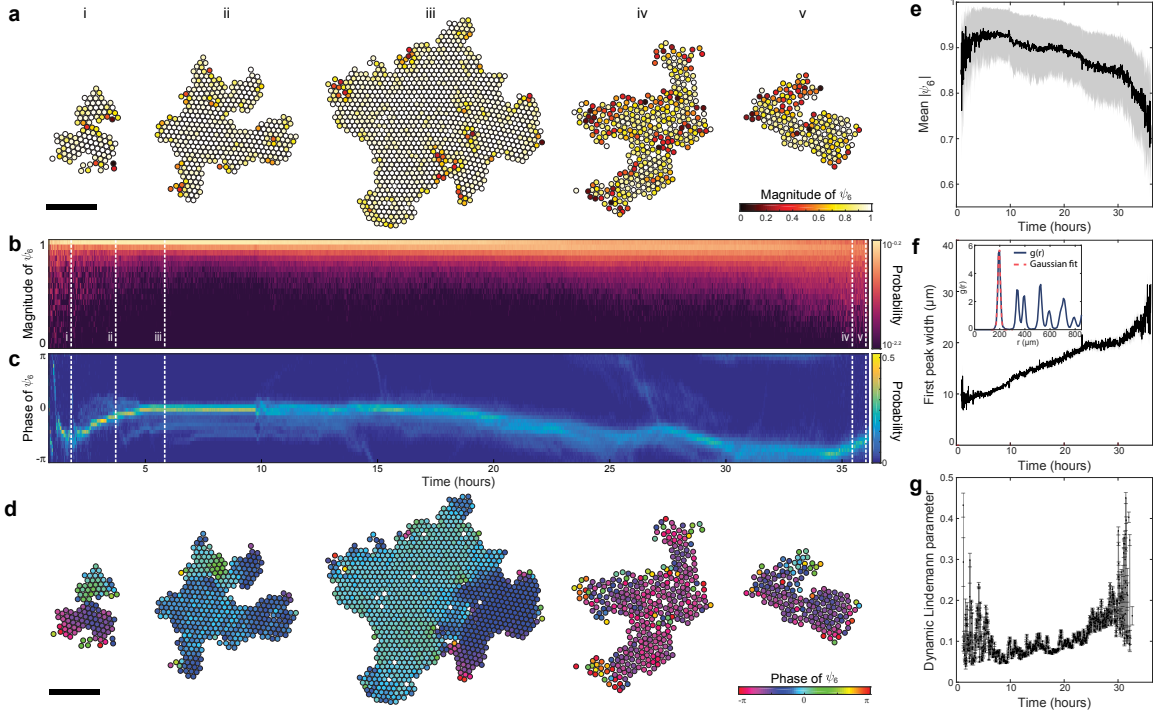


**Figure 3: Crystalline order first increases and then decreases as embryos develop.** **a**, Embryo centroids at different time points color-coded by the magnitude of the orientational order parameter  $|\psi_6|$  (SI Sec. 3.4). Scale bar, 2mm. **b – c**, The measured probability distribution of  $|\psi_6|$  spreads to smaller values after about 20 hours, indicating a loss of bond-orientational order (**b**). The ensuing drift of the mean phase angle (**c**) signals dynamical restructuring of the crystal. **d**, Embryo centroids at different times color-coded by the phase of  $\psi_6$ . Scale bar, 2mm. Time slices corresponding to snapshots (i–v) in **a** and **d** are indicated by white dotted lines. **e**, Average magnitude of  $\psi_6$  decays after  $\sim 10$  hours, confirming a decrease in orientational order. Error bars indicate standard deviation. **f**, The widening of the first peak of the radial pair distribution function  $g(r)$  indicates increased variation in the distance between nearest neighbors. Error bars indicate 95% confidence interval from Gaussian fit. Inset: Example pair distribution function,  $g(r)$ , and Gaussian fit to the first peak (SI Sec. 3.5). **g**, The increase of the dynamic Lindemann parameter with developmental time signals a progressive destabilization of the crystal lattice. Error bars indicate standard deviation of 20 consecutive time points (SI Sec. 3.6).

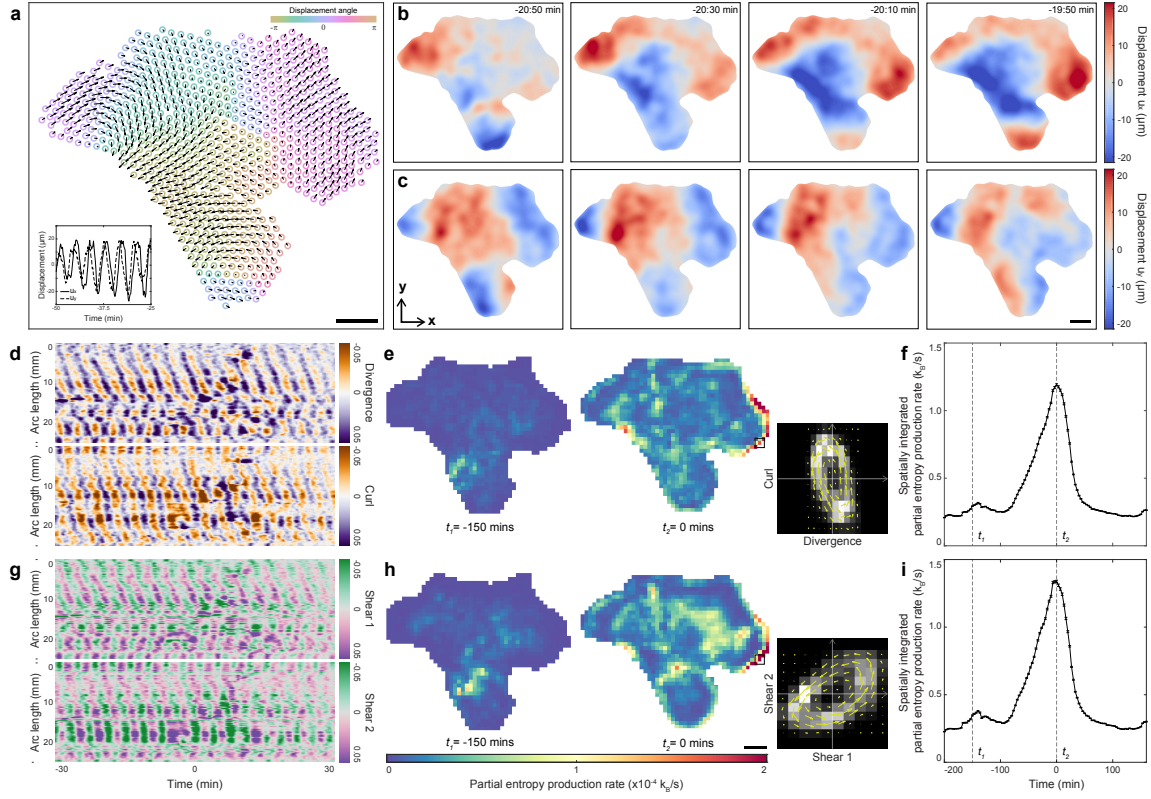


**Figure 4: Chiral displacement waves exhibit signatures of odd elasticity.** **a**, Instantaneous embryo centroid displacements from their time-averaged mean positions in the cluster (SI Sec. 3.7). Colors indicate the orientation of the displacement vector. Inset:  $x$  and  $y$  components of the displacement of a representative embryo, indicating robust oscillations with frequency  $\approx 0.26 \text{ min}^{-1}$  (SI Sec. 3.7). Scale bar, 1 mm. **b–c**, Snapshots of the  $x$  and  $y$  components of the displacement field  $\mathbf{u}(\mathbf{r}, t)$  as seen in a frame co-rotating with the crystal. Scale bar, 1 mm. **d**, Space-time kymographs of the boundary divergence and curl. **e**, Spatial maps of the partial entropy production rate computed from divergence-curl cycles during periods of low ( $t_1$ ) and high ( $t_2$ ) activity (SI Sec. 3.9). Scale bar, 1 mm. Inset: Density current plot in the divergence-curl phase space, computed at the location of the black box, showing a representative strain cycle. **f**, Spatially integrated entropy production rate obtained by integrating contributions from the local divergence-curl cycles. Error bars indicate standard deviation over 100 bootstraps (SI Sec. 3.9). Time point of maximum entropy production rate  $t_2$  is defined as 0 min. **g–i**, Performing an analogous analysis for the pair of shear components, shear 1 and shear 2, yields results consistent with those in **d–f**.

indicating that these modes are directly linked to the spinning motion of the embryos.

Both the non-reciprocal pair interactions between embryos and the emergence of self-sustained chiral waves are phenomenologically consistent with recent theoretical predictions for odd elastic materials [36]. Another predicted feature of odd elasticity is the appearance of quasistatic strain and shear cycles, from which work can be extracted [36]. To investigate whether such cycles may appear in our LCC system, we determined the displacement gradient tensor,  $u_{\alpha\beta} = \partial u_\alpha / \partial r_\beta$ , and extracted the four principal strain components (SI Sec. 3.7): divergence ( $u_{xx} + u_{yy}$ ), curl ( $u_{yx} - u_{xy}$ ), shear 1 ( $u_{xx} - u_{yy}$ ) and shear 2 ( $u_{yx} + u_{xy}$ ). All four quantities exhibit sustained periods of oscillation, as evident from kymographs that were computed in the local normal-tangent coordinate frames along the boundary (Fig. 4d,g, SI Sec. 3.7). Moreover, two-dimensional phase space plots of values of divergence-curl pairs and shear 1-shear 2 pairs, respectively, reveal self-sustained strain cycles (Fig. 4e,h, insets). Such strain cycles are theoretically predicted [36] signatures of non-equilibrium materials with odd elastic moduli,  $A$  and  $K^\circ$ , where  $A$  couples compression to an internal torque density and a nonzero  $K^\circ$  implies antisymmetric shear coupling.

Finite odd elastic moduli can give rise to work and dissipation cycles within emergent strain waves [36]. To quantify the lower bounds of the entropy production rates associated with strain cycles, we estimated the statistical irreversibility of the observed cycles using recently developed frameworks of stochastic thermodynamics [5, 24]. By calculating the phase-space currents for each embryo's smoothed position in the LCC, we constructed spatial maps of the local entropy production rates arising from the divergence-curl couplings (Fig. 4e, SI Sec. 3.9) and shear 1-shear 2 couplings (Fig. 4h), respectively. These maps reveal spatio-temporal variations of the entropy production rates, with higher rates appearing mostly in the vicinity of vacancy defects and boundary regions where embryos can move more freely. The spatially integrated entropy production rates for both the divergence-curl cycles and the shear 1-shear 2 cycles, over the entire area of the crystal, exhibit temporal maxima during the period of most active wave propagation (Fig. 4f,i). This observation is consistent with the predicted behavior of odd elastic materials [36].

## Discussion

Our combined experimental and theoretical analyses demonstrate how developmentally driven processes in marine multicellular organisms can lead to the emergence and destruction of collective crystalline order. By observing starfish embryos over two days post gastrulation, we have identified the hydrodynamic mechanisms that facilitate the formation of living crystals. More broadly, these results demonstrate how chiral symmetry breaking at the single-organism level combined with non-reciprocal hydrodynamic and steric interactions can give rise to self-sustained chiral waves that carry signatures of odd elasticity. Multicellular systems naturally break time-reversal and often chiral symmetries. We therefore hypothesize that the nonequilibrium phenomena reported here can be generalized to other living systems, such as volvocine green algae [17] and epithelial tissues [15].

## Acknowledgments

We thank William Irvine, Ned Wingreen, Jinghui Liu and Yu-Chen Chao for helpful discussions. N.F., J.D. and S.G. are grateful to KITP program ‘ACTIVE20: Symmetry, Thermodynamics and Topology in Active Matter’. This research was supported by the National Science Foundation CAREER Award (to N.F.). This research was supported in part by the National Science Foundation under grant no. NSF PHY-1748958. T.H.T. acknowledges support from the NSF-Simons Center for Mathematical and Statistical Analysis of Biology at Harvard (award number 1764269) and Harvard Quantitative Biology Initiative as NSF-Simons Postdoctoral Fellow. T.H.T. acknowledges support from the Center for Systems Biology Dresden as ELBE Postdoctoral Fellow. A.M. acknowledges support from a Longterm Fellowship from the European Molecular Biology Organization (ALTF 528-2019) and a Postdoctoral Research Fellowship from the Deutsche Forschungsgemeinschaft (Project 431144836). Y.C. acknowledges support from MIT Department of Physics Curtis Marble Fellowship. P.J.F. and S.G. acknowledge support from the Gordon and Betty Moore Foundation as Physics of Living Systems Fellows through grant no. GBMF4513. J.D. was supported by the Robert E. Collins Distinguished Scholarship fund. We thank the MIT SuperCloud [33] for providing access to its HPC resources.

## References

- [1] P. W. Anderson. More is different. *Science*, 177(4047):393–396, 1972.
- [2] N. W. Ashcroft and N. Mermin. *Solid state physics*, volume 2005. Saunders, 1976.
- [3] J. Avron. Odd viscosity. *J. Stat. Phys.*, 92(3):543–557, 1998.
- [4] D. Banerjee, V. Vitelli, F. Jülicher, and P. Surówka. Active viscoelasticity of odd materials. *Phys. Rev. Lett.*, 126(13):138001, 2021.
- [5] C. Battle, C. P. Broedersz, N. Fakhri, V. F. Geyer, J. Howard, C. F. Schmidt, and F. C. MacKintosh. Broken detailed balance at mesoscopic scales in active biological systems. *Science*, 352(6285):604–607, 2016.
- [6] T. Bäuerle, R. C. Löffler, and C. Bechinger. Formation of stable and responsive collective states in suspensions of active colloids. *Nat. Comm.*, 11(1):2547, 2020.
- [7] D. Bi, J. H. Lopez, J. M. Schwarz, and M. L. Manning. A density-independent rigidity transition in biological tissues. *Nat. Phys.*, 11(12):1074–1079, 2015.
- [8] W. Bialek, A. Cavagna, I. Giardina, T. Mora, E. Silvestri, M. Viale, and A. M. Walczak. Statistical mechanics for natural flocks of birds. *Proc. Natl. Acad. Sci. U.S.A.*, 109(13):4786–4791, 2012.
- [9] E. S. Bililign, F. B. Usabiaga, Y. A. Ganan, V. Soni, S. Magkiriadou, M. J. Shelley, D. Bartolo, and W. Irvine. Chiral crystals self-knead into whorls. *Preprint at arXiv:2102.03263*, 2021.
- [10] A. Bricard, J.-B. Caussin, N. Desreumaux, O. Dauchot, and D. Bartolo. Emergence of macroscopic directed motion in populations of motile colloids. *Nature*, 503:95–98, 2013.
- [11] M. E. Cates and J. Tailleur. Motility-induced phase separation. *Annu. Rev. Condens. Matter Phys.*, 6(1):219–244, 2015.
- [12] C. Collinet and T. Lecuit. Programmed and self-organized flow of information during morphogenesis. *Nat. Rev. Mol. Cell Biol.*, 22(4):245–265, 2021.

- [13] K. Drescher, R. E. Goldstein, N. Michel, M. Polin, and I. Tuval. Direct measurement of the flow field around swimming microorganisms. *Phys. Rev. Lett.*, 105:168101, 2010.
- [14] K. Drescher, K. C. Leptos, I. Tuval, T. Ishikawa, T. J. Pedley, and R. E. Goldstein. Dancing Volvox: Hydrodynamic Bound States of Swimming Algae. *Phys. Rev. Lett.*, 102:168101, 2009.
- [15] G. Duclos, C. Blanch-Mercader, V. Yashunsky, G. Salbreux, J.-F. Joanny, J. Prost, and P. Silberzan. Spontaneous shear flow in confined cellular nematics. *Nat. Phys.*, 14(7):728–732, 2018.
- [16] W. Gilpin, V. N. Prakash, and M. Prakash. Vortex arrays and ciliary tangles underlie the feeding–swimming trade-off in starfish larvae. *Nat. Phys.*, 13(4):380–386, 2017.
- [17] R. E. Goldstein. Green algae as model organisms for biological fluid dynamics. *Annu. Rev. Fluid Mech.*, 47(1):343–375, 2015.
- [18] B. A. Grzybowski, H. A. Stone, and G. M. Whitesides. Dynamic self-assembly of magnetized, millimetre-sized objects rotating at a liquid–air interface. *Nature*, 405(6790):1033–1036, 2000.
- [19] R. Hartmann, P. K. Singh, P. Pearce, R. Mok, B. Song, F. Díaz-Pascual, J. Dunkel, and K. Drescher. Emergence of three-dimensional order and structure in growing biofilms. *Nat. Phys.*, 15(3):251, 2019.
- [20] T. Ishikawa, T. J. Pedley, K. Drescher, and R. E. Goldstein. Stability of dancing volvox. *J. Fluid Mech.*, 903:A11, 2020.
- [21] A. J. Koch and H. Meinhardt. Biological pattern formation: from basic mechanisms to complex structures. *Rev. Mod. Phys.*, 66:1481–1507, 1994.
- [22] E. Lauga. *The Fluid Dynamics of Cell Motility*. Cambridge Texts in Applied Mathematics. Cambridge University Press, 2020.
- [23] W. Lee, H. Amini, H. A. Stone, and D. Di Carlo. Dynamic self-assembly and control of microfluidic particle crystals. *Proc. Natl. Acad. Sci. U.S.A.*, 107(52):22413–22418, 2010.
- [24] J. Li, J. M. Horowitz, T. R. Gingrich, and N. Fakhri. Quantifying dissipation using fluctuating currents. *Nat. Comm.*, 10(1666), 2019.
- [25] R. Li and B. Bowerman. Symmetry breaking in biology. *Cold Spring Harb. Perspect. Biol.*, 2(3):a003475, 2010.
- [26] M. C. Marchetti, J. F. Joanny, S. Ramaswamy, T. B. Liverpool, J. Prost, M. Rao, and R. A. Simha. Hydrodynamics of soft active matter. *Rev. Mod. Phys.*, 85(3):1143–1189, 2013.
- [27] S. R. Naganathan, S. Fürthauer, M. Nishikawa, F. Jülicher, and S. W. Grill. Active torque generation by the actomyosin cell cortex drives left–right symmetry breaking. *eLife*, 3:e04165, 2014.
- [28] D. R. Nelson and B. Halperin. Dislocation-mediated melting in two dimensions. *Phys. Rev. B*, 19(5):2457, 1979.
- [29] J. Palacci, S. Sacanna, A. P. Steinberg, D. J. Pine, and P. M. Chaikin. Living Crystals of Light-Activated Colloidal Surfers. *Science*, 339(6122):936–940, 2013.
- [30] A. P. Petroff and A. Libchaber. Nucleation of rotating crystals by Thiovulum majus bacteria. *New J. Phys.*, 20(1):015007, 2018.

- [31] A. P. Petroff, X.-L. Wu, and A. Libchaber. Fast-moving bacteria self-organize into active two-dimensional crystals of rotating cells. *Phys. Rev. Lett.*, 114:158102, 2015.
- [32] B. Qin, C. Fei, A. A. Bridges, A. A. Mashruwala, H. A. Stone, N. S. Wingreen, and B. L. Bassler. Cell position fates and collective fountain flow in bacterial biofilms revealed by light-sheet microscopy. *Science*, 369(6499):71–77, 2020.
- [33] A. Reuther, J. Kepner, C. Byun, S. Samsi, W. Arcand, D. Bestor, B. Bergeron, V. Gadepally, M. Houle, M. Hubbell, et al. Interactive supercomputing on 40,000 cores for machine learning and data analysis. *IEEE High Perf. Ext. Comp. Conf.*, 1:1–6, 2018.
- [34] I. H. Riedel, K. Kruse, and J. Howard. A self-organized vortex array of hydrodynamically entrained sperm cells. *Science*, 309(5732):300–303, 2005.
- [35] S. B. Rosenthal, C. R. Twomey, A. T. Hartnett, H. S. Wu, and I. D. Couzin. Revealing the hidden networks of interaction in mobile animal groups allows prediction of complex behavioral contagion. *Proc. Natl. Acad. Sci. U.S.A.*, 112(15):4690–4695, 2015.
- [36] C. Scheibner, A. Souslov, D. Banerjee, P. Surówka, W. T. M. Irvine, and V. Vitelli. Odd elasticity. *Nat. Phys.*, 16(4):475–480, 2020.
- [37] S. Shankar, A. Souslov, M. J. Bowick, M. C. Marchetti, and V. Vitelli. Topological active matter. *Preprint at arXiv:2010.00364*, 2020.
- [38] Z. Shen, A. Würger, and J. S. Lintuvuori. Hydrodynamic self-assembly of active colloids: chiral spinners and dynamic crystals. *Soft Matter*, 15:1508–1521, 2019.
- [39] D. J. Smith, T. D. Montenegro-Johnson, and S. S. Lopes. Symmetry-breaking cilia-driven flow in embryogenesis. *Annu. Rev. Fluid Mech.*, 51(1):105–128, 2019.
- [40] A. Sokolov, I. S. Aranson, J. O. Kessler, and R. E. Goldstein. Concentration dependence of the collective dynamics of swimming bacteria. *Phys. Rev. Lett.*, 98:158102, 2007.
- [41] V. Soni, E. S. Bililign, S. Magkiriadou, S. Sacanna, D. Bartolo, M. J. Shelley, and W. T. Irvine. The odd free surface flows of a colloidal chiral fluid. *Nat. Phys.*, 15(11):1188–1194, 2019.
- [42] K. Y. Wan, S. K. Hürlimann, A. M. Fenix, R. M. McGillivray, T. Makushok, E. Burns, J. Y. Sheung, and W. F. Marshall. Reorganization of complex ciliary flows around regenerating stentor coeruleus. *Philos. Trans. R. Soc. B*, 375(1792):20190167, 2020.
- [43] G. Wang, T. V. Phan, S. Li, M. Wombacher, J. Qu, Y. Peng, G. Chen, D. I. Goldman, S. A. Levin, R. H. Austin, et al. Emergent field-driven robot swarm states. *Phys. Rev. Lett.*, 126(10):108002, 2021.
- [44] K. Zahn and G. Maret. Dynamic criteria for melting in two dimensions. *Phys. Rev. Lett.*, 85(17):3656, 2000.

# Supplementary Information

## Development drives dynamics of living chiral crystals

Tzer Han Tan<sup>1,2,5</sup>, Alexander Mietke<sup>3,5</sup>, Hugh Higinbotham<sup>4,6</sup>, Junang Li<sup>4,6</sup>, Yuchao Chen<sup>4</sup>, Peter J. Foster<sup>4</sup>, Shreyas Gokhale<sup>4</sup>, Jörn Dunkel<sup>3</sup>, Nikta Fakhri<sup>4,7</sup>

<sup>1</sup> Quantitative Biology Initiative, Harvard University, Cambridge, MA, USA

<sup>2</sup> Center for Systems Biology Dresden, Dresden, Germany

<sup>3</sup> Department of Mathematics, Massachusetts Institute of Technology, Cambridge, MA, USA

<sup>4</sup> Department of Physics, Massachusetts Institute of Technology, Cambridge, MA, USA

<sup>5</sup> These authors contributed equally and are joint first authors.

<sup>6</sup> These authors contributed equally.

<sup>7</sup> Corresponding authors: fakhri@mit.edu

<b>1 Experiment</b>	<b>2</b>
1.1 Preparation of starfish embryos . . . . .	2
1.2 Clustering and flow field experiments . . . . .	2
1.3 Sedimentation of inactive embryos . . . . .	2
<b>2 Theory</b>	<b>2</b>
2.1 Hydrodynamics of a single embryo below the fluid surface . . . . .	3
2.1.1 Stokeslet description of bound states . . . . .	3
2.1.2 Stability of bound states and hydrodynamic focusing in wells . . . . .	3
2.2 Minimal model of cluster formation and rotation . . . . .	6
2.2.1 Force and torque balance . . . . .	6
2.2.2 Determining model parameters from experimental data . . . . .	8
2.2.3 Details of numerical simulations . . . . .	9
2.3 Discussion . . . . .	10
<b>3 Data Analysis</b>	<b>11</b>
3.1 Starfish embryo centroid localization and rotation correction . . . . .	11
3.2 Analysis of flow fields surrounding free spinning embryos, pairs and triplets . . . . .	11
3.2.1 Flow field measurements . . . . .	11
3.2.2 Flow field fitting . . . . .	12
3.3 Embryo spinning frequencies . . . . .	14
3.4 Orientational order parameter . . . . .	14
3.5 Pair distribution function . . . . .	15
3.6 Dynamic Lindemann parameter . . . . .	16
3.7 Displacement field and strain components . . . . .	16
3.8 Mode chirality analysis of displacement waves . . . . .	17
3.9 Phase space current and partial entropy production . . . . .	18

# 1 Experiment

## 1.1 Preparation of starfish embryos

Starfish *Patiria Miniata* were procured from South Coast Bio-Marine LLC. The animals were kept in salt water fish tanks maintained at 15°C. To fertilize embryos, we first extracted oocytes and sperm separately. Ovaries were extracted through a small incision made at the bottom of the starfish and were then carefully fragmented using a pair of scissors to release the oocytes. Extracted oocytes were washed twice with calcium free seawater to prevent maturation and incubated in artificial filtered seawater (FSW) at 15°C. The testes were extracted similarly and kept in a 1 mL Eppendorf tube at 4°C. To fertilize embryos, we first matured the oocytes by adding the hormone 1-methyladenine. After one hour, sperm extract was added to the culture at a 1:10000 dilution. Fertilized embryos were cultured in FSW at 15°C for the first 24 hours before being moved to 20°C.

## 1.2 Clustering and flow field experiments

All experiments have been performed at 20°C. For clustering experiments, the appropriate number of embryos was transferred to a well of a 24 well plate (VWR sterilized tissue culture plates, Catalog Number 10861-558). Imaging was done using a dissection scope (Nikon SMZ745) with a high-speed CMOS digital camera (Amscope MU500) attached at the eyepiece position.

To measure flow fields around embryos, 1 μm sized polystyrene beads were added to the medium. Cross-sectional flow field experiments (Fig. 2a,b,d, main text) were performed with embryos oriented vertically near the water-air interface. The corresponding data analysis is detailed in Sec. 3.2. Transverse flow field experiments (Fig 1b, main text) were performed by confining embryos between two cover-slips with 100 μm space in between and imaging them using a Leica microscope (DMIL LED) with either a 10x/0.25 (N PLAN CY) or a 4x/0.10 (HI PLAN) objective. Embryo morphology images (Fig. 1b, main text) at different time points were obtained using the same experimental setup.

## 1.3 Sedimentation of inactive embryos

To estimate the embryo's negatively buoyant weight force  $F_g$ , we performed a sedimentation experiment. Embryos were immobilized by treatment with 1 mM Sodium Azide  $NaN_3$ , which is a metabolic inhibitor [10]. They were then transferred to a long Pasteur pipette (diameter 7 mm) and released from the top position. The process of immobilized embryo sedimentation was video-recorded and embryos were tracked to determine sedimentation velocities  $v_s$ . Finally, using the measured velocities,  $v_s = (0.6 \pm 0.1) \text{ mm/s}$  (mean ± standard deviation,  $n = 7$ ), together with effective embryo size  $L = 150 \mu\text{m}$ , a negatively buoyant weight force of  $F_g = (1.7 \pm 0.3) \text{ nN}$  was estimated from Stokes' law.

# 2 Theory

The length and time scales,  $L \sim 150 \mu\text{m}$  (typical embryo size) and  $u \sim 0.1 \text{ mm/s}$  (typical flow speed), relevant for the embryo dynamics correspond to a Reynolds number of  $\text{Re} \sim 1.5 \times 10^{-2}$  and therefore allow for a theoretical description of our system in terms of Stokesian hydrodynamics. For low-Reynolds number microswimmers it is well-established that their dynamics and hydrodynamic interactions can be modulated by nearby fluid-substrate interfaces [7, 22, 6, 21] or free fluid surfaces [14]. Building on the corresponding ideas, we aim to develop in this section a quantitative and mechanistic understanding of how starfish embryos form stable surface bound states and how interactions between them lead to the observed phenomenology of cluster formation.

## 2.1 Hydrodynamics of a single embryo below the fluid surface

For the following analysis, we consider a coordinate system with its origin located on the fluid surface and the  $z$ -axis aligned with the surface normal pointing away from the fluid. When bound and spinning near the surface, single embryos move only very slowly in the  $xy$ -plane, as compared to their free propagation speed in the bulk fluid. Hence, we fix the embryo's effective hydrodynamic center for the following analysis at position  $\mathbf{r}_0 = (x_0, y_0, -h)^\top$ , where  $h > 0$  is the distance below the surface. For simplicity, we do not take into account shape changes of the fluid surface due to the presence of embryos and treat it as a non-deforming and shear stress-free interface.

### 2.1.1 Stokeslet description of bound states

From sedimentation experiments (Sec. 1.3), we know that starfish embryos are negatively buoyant. When bound near the surface, the net force generated by ciliary beating must therefore compensate the negatively buoyant weight force. The generic flow profile around a force  $\mathbf{F} = (F_x, F_y, F_z)^\top$  located at  $\mathbf{r}_0$  in an unbound fluid is known as Stokeslet flow

$$\mathbf{u}_{st}(\mathbf{r}; \mathbf{F}, \mathbf{r}_0) = \frac{1}{8\pi\eta} \left( \frac{\mathbf{F}}{|\mathbf{r} - \mathbf{r}_0|} + \frac{\mathbf{F} \cdot (\mathbf{r} - \mathbf{r}_0)(\mathbf{r} - \mathbf{r}_0)}{|\mathbf{r} - \mathbf{r}_0|^3} \right), \quad (1)$$

where  $\eta$  denotes the fluid viscosity. For a force  $\mathbf{F}$  at  $\mathbf{r}_0$  that is applied below a non-deforming free surface at  $z = 0$ , i.e. near an interface with  $u_z|_{z=0} = 0$  and vanishing hydrodynamic shear stress components  $\sigma_{xy}|_{z=0} = \sigma_{xz}|_{z=0} = 0$ , the flow field at any point  $\mathbf{r} = (x, y, z)^\top$  with  $z \leq 0$  is given by [14]

$$\bar{\mathbf{u}}_{st}(\mathbf{r}; \mathbf{F}, \mathbf{r}_0) = \mathbf{u}_{st}(\mathbf{r}; \mathbf{F}, \mathbf{r}_0) + \mathbf{u}_{st}(\mathbf{r}; \mathbf{F}', \mathbf{r}'_0), \quad (2)$$

where  $\mathbf{F}' = (F_x, F_y, -F_z)^\top$  and  $\mathbf{r}'_0 = (x_0, y_0, h)^\top$ . The second term in Eq. (2) corresponds to an image Stokeslet placed above the surface, which enforces the non-deforming free surface boundary conditions at  $z = 0$ , i.e. at all points  $\mathbf{r} = (x, y, 0)^\top$ .

Flow fields in the  $xy$ -plane that are generated by bound embryos are well-described by the Stokeslet flow given in Eq. (2) (Fig. 2b, main text). Furthermore, the Stokeslet strength  $F_{st} = |\mathbf{F}| = (2.6 \pm 0.3) \text{ nN}$  (Fig. S1a) determined from the corresponding fits (see Sec. 3.2.2 for fitting procedure) is comparable to the negatively buoyant weight force  $F_g = (1.7 \pm 0.3) \text{ nN}$  estimated from sedimentation experiments (Sec. 1.3). The fact that  $F_{st} > F_g$  shows that the ciliary activity generates sufficient buoyancy to overcome the negatively buoyant weight force. It also suggests that the fluid's surface tension generates a small counter-force  $F_\sigma = F_{st} - F_g$  that allows embryos to stay net force-free at a constant distance  $h$  below the surface.

The flow described by Eq. (2) as seen in a ‘side-view’ in the  $xz$ -plane is shown in Fig. S1b. As in the case of Stokeslet flow below a rigid surface [22, 6], a strong lateral inwards flow will draw in nearby embryos and thereby generate an effective attraction between them. We will use this fact below to describe the attraction between embryos in a minimal hydrodynamic model (Sec. 2.2).

Finally, we note that the embryo's spinning motion around its own AP-axis as such has no substantial effect on the surrounding fluid flow. In fact, an axisymmetric surface that generates a net torque on the surrounding fluid through a constant surface force density will spin at a frequency that is set by the rotational drag. In an unbound low-Reynolds number fluid, this steady state will not generate any flow of the surrounding fluid, a fact that remains valid in the vicinity of a non-deforming shear stress-free interface.

### 2.1.2 Stability of bound states and hydrodynamic focusing in wells

The experimental observation that single starfish embryos form long-lived bound states near the fluid surface suggests a hydrodynamic stabilization of such states. To rationalize this, we next studied how the embryo's body axis  $\mathbf{p}$ , a unit vector pointing from posterior to anterior, interacts

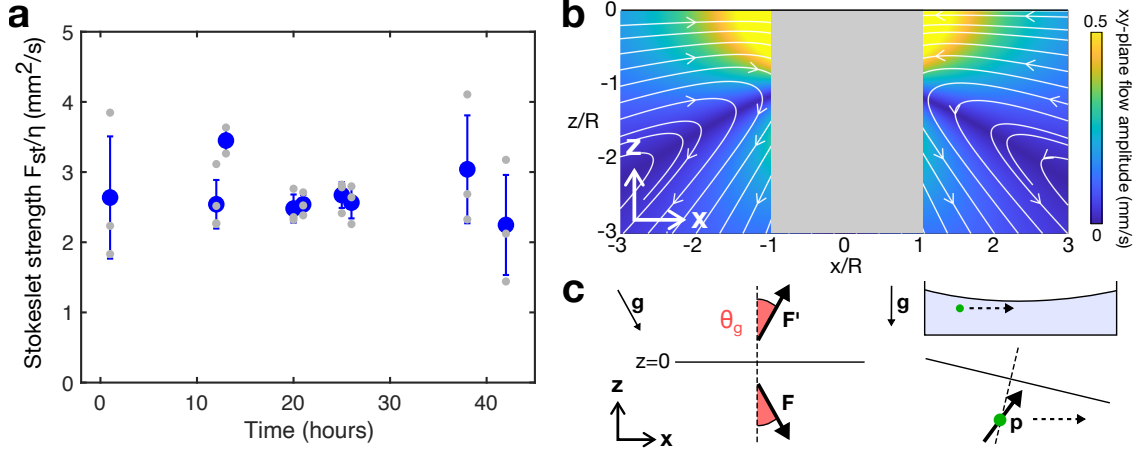


Figure S1: **Hydrodynamics of single embryos bound below a free fluid surface.**

**a**, Stokeslet strength  $F_{st}$  normalized by fluid viscosity  $\eta$  from fits of in-plane flow fields (Sec. 3.2.2) over time course of experiments. Gray dots depict individual fit values, blue dots and error bars represent mean and standard deviation, respectively. **b**, Side-view of Stokeslet flow below a free surface (Eq. (2) with  $\mathbf{r}_0 = (0, 0, -R)^\top$ ,  $F_{st}/\eta = 2.6 \text{ mm}^2/\text{s}$ ,  $R = 110 \mu\text{m}$ ). White lines depict stream lines in the  $xz$ -plane and colors indicate the amplitude of flows parallel to the  $xy$ -plane. The dominantly lateral in-flow leads to an effective attraction between embryos. **c**, Image Stokeslet construction below a free surface ( $z = 0$ ) that allows for an angle  $\theta_g$  between surface normal and gravity  $\mathbf{g}$  (left) to represent embryos below a curved fluid surface present in small wells (right). Stokeslet flow below a free surface provides a hydrodynamic self-stabilization of upright embryo orientations  $\mathbf{p}$ . Under a surface that is locally not orthogonal to gravity, a tilted stationary orientation enhances the accumulation of embryos near the well center (Sec. 2.1.2).

with its own Stokeslet flow below a free surface. To this end, we use the generalized Faxen's law for a prolate ellipsoidal body [12, 21]

$$\frac{d\mathbf{p}}{dt} = \frac{1}{2} [\nabla \times \mathbf{u}'(\mathbf{r}_0)] \times \mathbf{p} + \Gamma[\mathbf{p} \times (\mathbf{E}'(\mathbf{r}_0) \cdot \mathbf{p})] \times \mathbf{p}, \quad (3)$$

which describes the dynamics of the body axis orientation in response to external or image flow contributions  $\mathbf{u}'$ . The corresponding strain rate tensor is given by  $\mathbf{E}' = [\nabla \mathbf{u}' + (\nabla \mathbf{u}')^\top]/2$ . The geometric parameter  $\Gamma = (1 - e^2)/(1 + e^2)$ , with  $e = \ell_{min}/\ell_{maj}$  being the minor ( $\ell_{min}$ ) to major axis ( $\ell_{maj}$ ) ratio, captures shape anisotropies of the immersed body and vanishes for a sphere. The body axis  $\mathbf{p}$  points along the major axis. For a single embryo, we only require the Stokeslet image flow contributions  $\mathbf{u}'(\mathbf{r}) = \mathbf{u}_{st}(\mathbf{r}; \mathbf{F}', \mathbf{r}_0')$  evaluated at  $\mathbf{r} = \mathbf{r}_0 = (x, y, -h)^\top$ , for which Eq. (3) yields

$$\frac{d\mathbf{p}}{dt} = \frac{1}{8\pi\eta} \left( \frac{(\mathbf{p} \cdot \mathbf{F}') \mathbf{R} - (\mathbf{p} \cdot \mathbf{R}) \mathbf{F}'}{|\mathbf{R}|^3} + 3\Gamma (\mathbf{F}' \cdot \mathbf{R}) (\mathbf{p} \cdot \mathbf{R}) \frac{(\mathbf{p} \cdot \mathbf{R}) \mathbf{p} - \mathbf{R}}{|\mathbf{R}|^5} \right), \quad (4)$$

where  $\mathbf{R} = (0, 0, -2h)^\top$ . To define the orientation of the image Stokeslet force  $\mathbf{F}'$ , we take into account that capillary forces at boundaries of the wells in which embryos are suspended can lead to a finite curvature of the fluid-air interface. In this case, gravity is not everywhere aligned with the surface normal, but instead may be tilted by a relative angle  $\theta_g$ . Without loss of generality, we can write the image Stokeslet force as  $\mathbf{F}' = F_{st}(\sin \theta_g, 0, \cos \theta_g)^\top$ , where  $F_{st} > 0$  is the Stokeslet strength (Fig. S1c, left). Gravity is aligned with the surface normal for  $\theta_g = 0$ . Here, we assumed that the Stokeslet thrust  $F_{st} = |\mathbf{F}| = |\mathbf{F}'|$  generated by the embryo is independent of  $\mathbf{p}$ , as we are only interested in small tilts away from the stationary mean orientation. From Eq. (4) the dynamic

equation for each component of the orientation vector  $\mathbf{p}$  then follows as

$$\frac{dp_x}{dt} = \frac{F_{st}}{32\pi\eta h^2} (p_z \sin \theta_g - 3\Gamma p_z^2 p_x \cos \theta_g) \quad (5a)$$

$$\frac{dp_y}{dt} = -\frac{F_{st}}{32\pi\eta h^2} 3\Gamma p_z^2 p_y \cos \theta_g \quad (5b)$$

$$\frac{dp_z}{dt} = \frac{F_{st}}{32\pi\eta h^2} [-p_x \sin \theta_g + 3\Gamma (1 - p_z^2) p_z \cos \theta_g]. \quad (5c)$$

The stationary orientation of interest ( $\mathbf{p}$  mostly oriented along the  $z$ -axis) described by Eqs. (5) is given by

$$p_x^{(0)} = \frac{\tan \theta_g}{3\Gamma p_z^{(0)}} \quad (6a)$$

$$p_z^{(0)} = \sqrt{\frac{1}{2} + \sqrt{\frac{1}{4} - \left(\frac{\tan \theta_g}{3\Gamma}\right)^2}}, \quad (6b)$$

and  $p_y^{(0)} = 0$ , which shows that the body axis  $\mathbf{p}$  is at steady state oriented in the plane formed by the surface normal and the direction of gravity. Additional stationary solutions of Eqs. (5) exist. However, they are either linearly unstable (solutions for which  $\mathbf{p}^{(0)}$  is exactly or nearly parallel to the  $xy$ -plane) or represent orientations for which embryos are expected to push themselves away from the surface ( $\mathbf{p}^{(0)} \approx -\mathbf{e}_z$ ). For the relevant solution Eq. (6), two key scenarios can be discussed:

- *Gravity aligned with the surface normal ( $\theta_g = 0$ ): Stability of bound states*

In this case, only terms  $\sim \Gamma$  remain in Eqs. (5). Hence, below a free surface, only the axis  $\mathbf{p}$  of a geometrically anisotropic body ( $\Gamma \neq 0$ ) can be reoriented by its own Stokeslet flow, which is consistent with the observed elongated embryo morphologies (Fig. 1b, main text). Furthermore, the stationary orientation Eqs. (6) simplifies for  $\theta_g = 0$  to  $\mathbf{p}^{(0)} = \mathbf{e}_z$ , representing an embryo oriented upright below the free surface. From Eqs. (5a) and (5b) it directly follows that this state is linearly stable under a perturbation  $\delta\mathbf{p} = (\cos \phi \mathbf{e}_x + \sin \phi \mathbf{e}_y) \delta\theta$  for some 2D polar angle  $\phi$  and orientation perturbation  $\delta\theta$ . In particular, the linear dynamics is given by  $d\delta\theta/dt = -\delta\theta/\tau_\theta$  and defines a reorientation time-scale

$$\tau_\theta = \frac{32\pi\eta h^2}{3\Gamma F_{st}}. \quad (7)$$

For embryos in the middle of our experimental time window, around 26 h (see Fig. 1b), we have  $\ell_{maj} \approx 180 \mu\text{m}$ ,  $\ell_{min} \approx 110 \mu\text{m}$  ( $\Rightarrow \Gamma \approx 0.45$ ),  $h \approx \ell_{maj}$  and  $F_{st}/\eta \approx 2.6 \text{ mm}^2/\text{s}$ , such that  $\tau_\theta \approx 0.9 \text{ s}$ . This is smaller than, but still comparable to, the fluid flow timescale  $\tau_u = L/u \approx 1.5 \text{ s}$  (typical embryo size  $L \sim 150 \mu\text{m}$ , typical flow speeds  $u \sim 0.1 \text{ mm/s}$ ), suggesting that limited, but sufficient robustness is provided by this hydrodynamic self-stabilization. Other aspects, such as the bottom-heaviness of embryos, could enhance the stability of bound states further [6].

- *Gravity tilted relative to the surface normal ( $\theta_g \neq 0$ ): Hydrodynamic focusing in wells*

Embryos can be located beneath a non-leveled fluid surface for which  $\theta_g \neq 0$ . From Eq. (6b) it follows that a stationary solution only exist for anisotropic shapes with

$$\Gamma > \frac{3}{2} |\tan \theta_g|. \quad (8)$$

It can also be shown that bodies with smaller aspect ratios will instead undergo a steady tumbling motion. Furthermore, assuming Eq. (8) holds, we see from Eqs. (6) that the

stationary orientation vector is itself tilted relative to the fluid surface normal ( $p_x^{(0)} \neq 0$ ). A linearization of Eqs. (5) around the stationary state Eqs. (6) for arbitrary  $\theta_g$  shows that such a tilted state is still linearly stable. This has important consequences for swimmers that are bound below a potentially curved fluid surface: Whenever embryos tilt relative to the surface above them, part of the thrust that is generated by ciliary beating is converted into translational motion parallel to the surface. The direction of this translation is set by the direction of the embryo tilt, which in turn is set by the orientation of gravity relative to the surface normal. From the sign of  $p_x^{(0)}$  given in Eq. (6a) it follows that the body axis tilt relative to the surface is always oriented such that, for a convexly curved fluid surface in a well, bound embryos tend to translate towards the center of the well (Fig. S1c, right). This hydrodynamic focusing leads to a stronger accumulation of embryos near the center of smaller wells, an effect that is exploited in experiments to enhance the formation of large clusters.

## 2.2 Minimal model of cluster formation and rotation

In this section, we describe a minimal model of interacting chiral disks that faithfully recapitulates the phenomenology of cluster formation and quantitatively accounts for experimentally observed single embryo spinning and whole cluster rotation frequencies (Fig. 2e–g, main text). Notably, over the course of each experiment, system properties spread over almost three orders of magnitude in frequencies and in the number of embryos contained in clusters. For simplicity, our model aims at a description of the effectively two-dimensional dynamics in the  $xy$ -plane of a fixed number of embryos that are bound below the surface. In this case, each embryo can be represented as a disk and lateral interactions can be described by effective force and torque balance equations.

### 2.2.1 Force and torque balance

Before formulating an effective force and torque balance equations for a given embryo, we qualitatively describe the minimal set of interactions expected in our living chiral crystal system. Besides a steric repulsion between nearby embryos, the essential lateral interactions are given by:

- *Hydrodynamic attraction*

The long-ranged radial in-flow from the Stokeslet generated by each embryo below a free surface, described in Sec. 2.1.1 and quantified in Fig. 2b (main text), entrains surrounding embryos and thereby leads to an effective attraction between them. An analogous effect near rigid no-slip interfaces has been studied in various theoretical and experimental settings [7, 22, 6, 17].

- *Transverse hydrodynamic force and torque exchange*

Two nearby rotating embryo surfaces will experience an additional exchange of forces and torques due to hydrodynamic near-field interactions [12, 6, 17] (see Fig. 2c, main text). In particular, transverse forces within the  $xy$ -plane due to the neighboring embryo's spinning effectively make a pair of embryos ‘roll’ on each other. Together with the Stokeslet attraction, this leads to an orbiting motion of groups of embryos. Similarly, each embryo is subject to torques due to the spinning of nearby embryos, which leads to a slow-down of individual embryo spinning frequencies (Fig. 2f, main text). Importantly, forces and torques contributing to these interactions are expected to affect the fluid flow around rotating groups of embryos in a particular fashion, a prediction that was independently verified by fitting suitable sets of Stokeslet singularities to measured flow fields (see Fig. 2d (main text), Fig. S3 and Sec. 3.2.2).

Representing an embryo  $i$  by a disk with centroid position  $\mathbf{r}_i = (x_i, y_i, -h)$ , the above interactions

translate into an effective force balance of the form

$$\frac{d\mathbf{r}_i}{dt} = \sum_{j \neq i} \left[ \bar{\mathbf{u}}_{st}(\mathbf{r}_i; \mathbf{F}, \mathbf{r}_j) + \frac{1}{\eta R} \mathbf{F}_{rep}(|\mathbf{r}_i - \mathbf{r}_j|) + R(\omega_i + \omega_j) F_{nf}(|\mathbf{r}_i - \mathbf{r}_j|) \hat{\mathbf{r}}_{ij} \times \mathbf{e}_z \right], \quad (9)$$

which describes an overdamped dynamics of the in-plane centroid coordinates,  $dx_i/dt$  and  $dy_i/dt$ . The first term captures the Stokeslet-mediated attraction through the flow  $\bar{\mathbf{u}}_{st}$  [Eq. (2)] generated by embryos at positions  $\mathbf{r}_j$ . The second term in Eq. (9) implements a steric repulsion between embryos of the form  $\mathbf{F}_{rep}(r) = -dV(r)/d\mathbf{r}$ , where  $r = |\mathbf{r}|$  and

$$V(r) = f_{rep} \left( \frac{R}{r} \right)^{12}. \quad (10)$$

Here,  $R$  is the average apparent radius of bound embryos when viewed along the  $z$ -axis from above the fluid surface and the effective repulsion force  $f_{rep}$  was inferred from experiments (Sec. 2.2.2). The last term in Eq. (9) introduces the transverse hydrodynamic near-field forces. This transverse force is proportional to the relative velocity  $R(\omega_i + \omega_j)$  of two nearby embryo surfaces, where  $\omega_i$  denotes the angular spinning frequency of embryo  $i$ .  $\omega_i > 0$  ( $\omega_i < 0$ ) corresponds to clockwise (counter-clockwise) single embryo spinning when viewed from above the fluid surface. The direction of the transverse force is orthogonal to the unit vector  $\hat{\mathbf{r}}_{ij} = (\mathbf{r}_i - \mathbf{r}_j)/|\mathbf{r}_i - \mathbf{r}_j|$  that points from the center of disk  $j$  to the center of disk  $i$ . The amplitude of the transverse force depends on the distance  $d_{ij} = |\mathbf{r}_i - \mathbf{r}_j| - 2R$  between embryo surfaces and takes the form

$$F_{nf}(|\mathbf{r}_i - \mathbf{r}_j|) = \begin{cases} f_0 \ln \frac{d_0}{d_{ij}} & (d_{ij} < d_0) \\ 0 & (d_{ij} \geq d_0) \end{cases}, \quad (11)$$

which uses an asymptotic result from lubrication theory [12, 6]. The phenomenological dimensionless parameter  $f_0$  characterizes the strength of the transverse force exchange and is determined from experiments (see Sec. 2.2.2).

Anticipating the formation of clusters in experiments, where hydrodynamic attraction gets screened by the presence of neighboring embryos, we distinguish two populations of disks depending on the size of clusters they are part of at a given moment in time: A disk  $i$  that is isolated or part of a small cluster of at most 3 disks interacts with all other disks  $j$  via  $\bar{\mathbf{u}}_{st}(\mathbf{r}_i; \mathbf{F}, \mathbf{r}_j)$  in Eq. (9). A disk  $i$  that is part of a cluster with more than 3 disks only experiences a Stokeslet-mediated attraction with disks  $j$  with  $|\mathbf{r}_i - \mathbf{r}_j| \leq 3.8R$ , such that hydrodynamic attraction in larger clusters is restricted to nearest and second nearest neighbors interactions.

To mimic the effect of hydrodynamic focusing of embryos towards the well center (see Sec. 2.1.2 and Fig. S1c) and facilitate the formation of a single large cluster in simulations within finite time, the contribution  $\mathbf{F}_w/(\eta R)$  from an effective external force  $\mathbf{F}_w = -\eta R t_w^{-1} (x_i^2 + y_i^2)^{-1/2} \times (\cos \phi_i, \sin \phi_i, 0)^\top$  with  $t_w = 15$  min and  $\tan \phi_i = y_i/x_i$  was added to Eq. (9). This effectively places the center of the well at the in-plane coordinate origin  $x = 0$  and  $y = 0$ .

This model is closed by a torque balance that describes the evolution of each embryo's spinning frequency. We consider a fully overdamped scenario, in which the torque balance corresponds to an algebraic condition that determines instantaneous spinning frequencies of each embryo and is given by

$$\omega_i = \omega_0 - \sum_{j \neq i} (\omega_i + \omega_j) T_{nf}(|\mathbf{r}_i - \mathbf{r}_j|). \quad (12)$$

Single bound embryos are spinning with angular frequency  $\omega_0$  and nearby embryos slow down each other's spinning. The distance dependence of the latter interaction is again inspired by lubrication theory [12], which suggests the form

$$T_{nf}(|\mathbf{r}_i - \mathbf{r}_j|) = \begin{cases} \tau_0 \ln \frac{d_0}{d_{ij}} & (d_{ij} < d_0) \\ 0 & (d_{ij} \geq d_0) \end{cases}, \quad (13)$$

for the near-field contribution in Eq. (12). In Eq. (13), we introduced a phenomenological dimensionless parameter  $\tau_0$  that characterizes the strength of the torques that slow down the spinning of nearby embryo.

### 2.2.2 Determining model parameters from experimental data

The parameters contained in this model can be systematically determined from experimental measurements and suitable fits to the dynamics of single embryos, rotating pairs and rotating triplets. Similar to the Stokeslet strength  $F_{st}$  (Fig. S1a), apparent radii  $R$  and spinning frequencies  $\omega_0/(2\pi)$  of isolated bound embryos are determined from direct single embryo measurements (Fig. S2a,b). While we noted a slight decrease of in-plane flow speeds around single embryos towards the very end of the experimental time window, none of these parameters showed substantial changes over about 40 h. For given size  $R$  and attraction characterized by  $F_{st}$ , the repulsive force strength  $f_{rep}$  in Eq. (10) sets the surface distance  $d_{ij}$  between equilibrated pairs of disks in the minimal model. This distance was measured in experiments ( $\approx 20 \mu\text{m}$ ) and  $f_{rep}$  was set accordingly. Finally, rotation frequencies of pairs and triplets (Fig. S2c) in experiments can be used to set the transverse force strength  $f_0$ , while reduced embryo spinning frequencies within pairs and triplets (Fig. 2f, main text) determine the lateral torque strength  $\tau_0$ . The final parameter values used in simulations of the emergent cluster formation are listed in Tab. 1.

Parameter	$R (\mu\text{m})$	$\frac{\omega_0}{2\pi} (\text{Hz})$	$F_{st} (\text{nN})$	$f_{rep} (\text{nN})$	$f_0$	$\tau_0$	$d_0/R$	$\eta (\text{mPa}\cdot\text{s})$
Value	110	$0.72 \pm 0.17$	$2.6 \pm 0.3$	$6.9 \pm 1.4$	0.05	0.12	0.5	1

Table 1: Parameters used in the minimal hydrodynamic model of cluster formation. The parameters  $\omega_0$ ,  $F_{st}$  and  $f_{rep}$  have been drawn from random distributions as described below to reflect the natural variability of embryo properties.

*Introducing variability of single embryo parameters in the minimal model:* Experimental measurements of bound single embryo properties (Figs. S1a and S2a,b) provide insights into the biological variability of microscopic parameters. Qualitatively, this parameter variability can be interpreted as a form of noise that is present in the system. Indeed, parameter variability in the minimal model increases the likelihood of more comprehensive neighbor rearrangements when clusters merge. In the absence of microscopic variability on the other hand, even small clusters formed in the minimal model are rather static in their shape and nearest-neighbor topology, which is in contrast to experimental observations. To include parameter variability into the model, we proceeded as follows. Isolated bound embryo spinning frequencies  $\omega_0/(2\pi)$  and Stokeslet strength  $F_{st}$  were sampled for each disk from a normal distribution with mean and standard deviation as determined from experiments (Tab. 1). To mimic a finite apparent size variability in a minimal fashion, we additionally sampled the repulsive force strength  $f_{rep}$  homogeneously from the interval given in Tab. 1. Finally, to restore reciprocity of attraction and repulsion between disks  $i$  and  $j$  for sampled parameters  $\beta_i$  and  $\beta_j$  (representing corresponding values of  $F_{st}$  or  $f_{rep}$ ), we symmetrized the linear coefficients of each pair-wise interaction in Eq. (9) as  $F_{st}, f_{rep} \rightarrow (\beta_i + \beta_j)/2$ .

*Phenomenological scaling of embryo spinning frequencies in large clusters:* The emergent dynamics that our minimal model gives rise to can be tested by comparing spinning frequencies of embryos within clusters and whole-cluster rotation frequencies with experiments. The minimal model reveals that, as more disks join a cluster, the average nearest-neighbor distance is reduced, which leads to a slow-down of embryo spinning frequencies within clusters due to torque exchanges. This causes a reduction in lateral force exchanges and, together with the increased drag experienced by larger clusters, slows down whole-cluster rotations (see Fig. 2f,g, main text). The interactions described in Eqs. (9) and (12) with parameters from Tab. 1 quantitatively match the corresponding

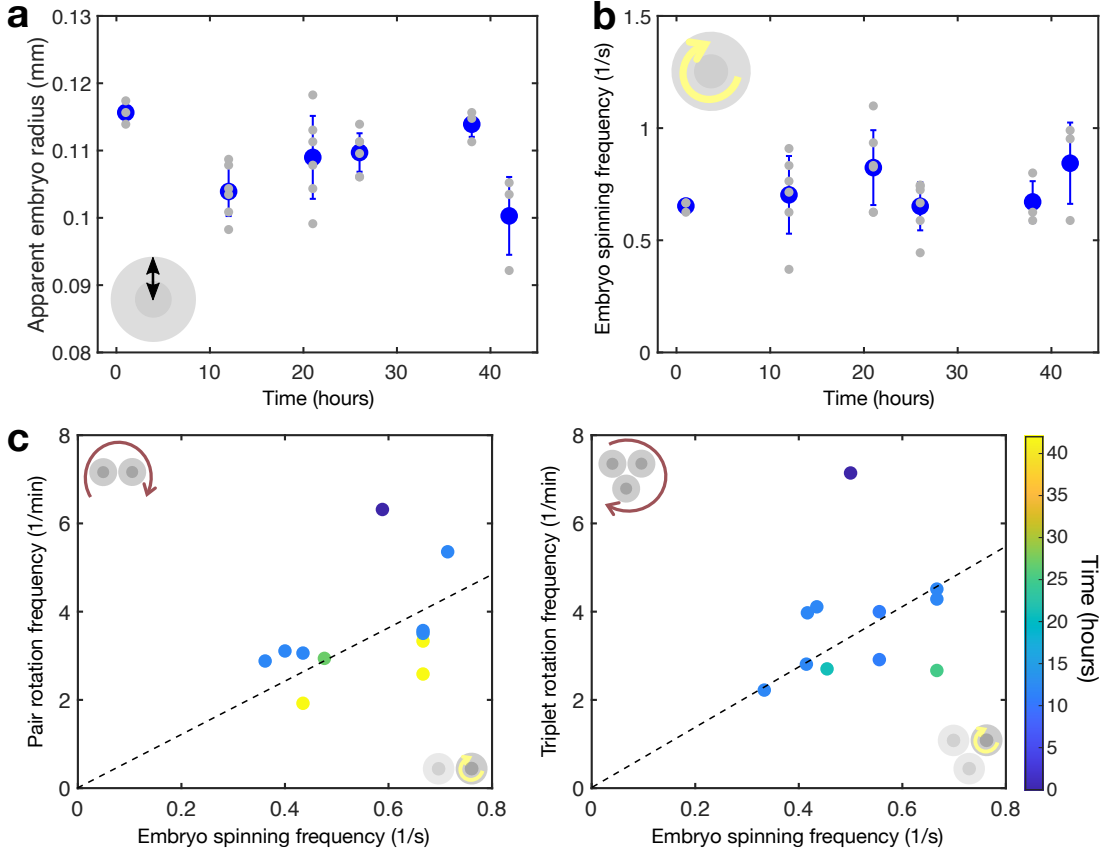


**Figure S2: Measurements of embryo properties.** **a,** Apparent radii  $R$  of embryos bound below the fluid surface. **b,** Spinning frequencies  $\omega_0/(2\pi)$  of isolated bound embryos. In **a** and **b**, gray dots depict single measurement values, blue dots and error bars represent mean and standard deviation, respectively. **c,** Rotation frequencies of bound pairs (left) and triplets (right) increase linearly with the spinning frequency of embryos within these groups, as previously observed for pairs of *Volvox* colonies [6]. Qualitatively, a given embryo spinning frequency translates over time into gradually smaller group rotation frequencies, suggesting a weakening of effective hydrodynamic interactions as development progresses. The variability of single embryo spinning frequencies (**b**) is consistent with the variability of spinning frequencies within pairs and triplets and consequently leads to variability in rotation frequencies of pairs and triplets. Black dashed lines depict calibration of average embryo properties in the minimal model (see Sec. 2.2).

experimental observations up to cluster sizes of about 60 to 70 embryos. For larger clusters, we observe experimentally a more drastic reduction in embryo spinning frequencies within clusters than captured by the local interactions described so far. To take this observation quantitatively into account, we introduced a phenomenological scaling of the form  $\omega_0 \rightarrow \omega_0/[1 + (N_{cl}/N_0)^2]$  into Eq. (12), where  $N_0 = 90$  and  $N_{cl}$  is the total number of disks in a given cluster.

### 2.2.3 Details of numerical simulations

The effective force and torque balance Eqs. (9) and (12) with parameters shown in Tab. 1 were implemented in MATLAB and solved using the ordinary differential equation solver `ode113`. Note that in practice Eq. (12) represents a separate linear system of equations for each connected

component of the graph that is generated by connecting all disks within a distance of  $|\mathbf{r}_i - \mathbf{r}_j| < d_0 + 2R$ . Because the weights of this linear system given by Eq. (13) depend only on positions  $\mathbf{r}_i$ , it can be explicitly solved for the angular spinning frequencies  $\omega_i$  at arbitrary intermediate time steps. The resulting values are directly used to evaluate the transverse force in Eq. (9).

To simulate the cluster formation shown in Fig. 2e (main text), we initiated 700 disks with individual parameters given in Tab. 1 and positioned them homogeneously on a circular domain with an approximate radius of 8 cm.

To determine the data shown in Fig. 2f (main text) ('In small clusters'), we ran 30 simulations of pairs, triplets and groups of four disks corresponding to one, two, and three direct neighbors, respectively. 10 simulations of clusters with 100 disks were run to determine spinning frequencies 'In large clusters' Fig. 2f (main text). Mean and standard deviations of the spinning frequencies extracted from these simulations are depicted by the symbols and error bars in Fig. 2f.

To determine the size-dependent whole-cluster rotation rates shown in Fig. 2g (main text), we ran 5 simulations for each total numbers of disks  $N_{cl} \in \{2, 3, 4, 5, 6, 7, 8, 9, 10, 12, 18, 27, 42, 63, 95, 144, 218, 330\}$  and extracted rotation frequencies of the final clusters that had formed. The standard variation of these whole-cluster rotation frequencies in the minimal model is smaller than the symbol size used in Fig. 2g (main text).

### 2.3 Discussion

While our minimal model quantitatively describes the formation and phenomenology of living chiral crystals over several orders of magnitude in cluster size, embryo spinning frequencies and cluster rotation frequencies (Fig. 2b,d–g, main text), several simplifications have been made that are briefly discussed in the following.

To simplify the fluid dynamics, we have assumed hydrodynamic interactions are dominated by the Stokeslet properties of single bound embryos. The corresponding singularity description was used to describe a fixed attraction strength among embryos and therefore neglects potential changes of the ciliary activity and more complex aspects of hydrodynamic interactions when embryos come closer together. Similarly, we have considered an isotropic potential-like steric repulsion in the  $xy$ -plane that reflects the mostly circular, apparent shapes of embryos bound below the surface. Taking more details of embryo morphology (Fig. 1b, main text) and associated hydrodynamic effects in tightly packed clusters faithfully into account will most likely require fully resolved, three-dimensional hydrodynamic simulations [20, 24], as well additional knowledge about the ciliary activity of embryos within clusters as compared to freely spinning ones.

We did not explicitly include contributions of cilia-cilia interactions between embryos that may become relevant when embryos within clusters get very close to each other. In particular, the latter effect could lead to additional terms that complement the hydrodynamically motivated transverse near-field force and torques given in Eqs. (11) and (13). Using the phenomenological coefficients  $f_0$  and  $\tau_0$  and determining them from experimental measurements (Sec. 2.2.2) partially accounts for this uncertainty. More generally, we restricted the force and torque balance equations to local interactions but note that hydrodynamic effects may lead, even among embryos within clusters, to effective long-ranged interactions. The phenomenological global scaling we introduced to quantitatively capture rotation frequencies of very large clusters could hint towards such a non-local effect.

For simplicity, we have considered a scenario with a constant number of interacting disks. In experiments, embryos at the clusters boundaries can depart from clusters and incoming embryos may fill up holes that arise, for example, when clusters merge. This additional level of effective noise in experiments smoothens 'sharp' edges of clusters, eliminates some of the vacancies or fills up larger holes that have formed, but it does otherwise not change the essential characteristics of cluster formation.

## 3 Data Analysis

This final section details the different data analysis approaches used to quantitatively characterize our experimental system.

### 3.1 Starfish embryo centroid localization and rotation correction

To identify starfish embryos, we first performed a circular Hough transform using the MATLAB (2016b, MathWorks) function `imfindcircles` on inverted raw intensities of microscopy images. To calculate the rotation frequency of clusters, we first identified all embryos within a cluster. This was done by recursively finding all nearest neighbors within a 1.5 embryo diameter from a predetermined seed position (for large clusters) or by using intensity thresholding to identify clusters and identifying the embryo centroids that lie within a given cluster region (for small clusters). Particle tracking was performed using Hungarian linker algorithm [13] (for large clusters) or Daniel Blair and Eric Dufresne's MATLAB adaptation of the IDL Particle Tracking software (for small clusters) [2]. The rotation angle between any two consecutive time points was calculated by finding a rigid body transformation that maximizes the overlap of the embryo centroid positions between two time frames. We then applied the inverse transformation on subsequent time frames to obtain embryo centroid positions in the cluster's co-rotating frame for analysis, which we refer to as *rotation-corrected* centroid data. Measured rotation frequencies of clusters as a function of the number of embryos are shown in Fig. 2g (main text).

### 3.2 Analysis of flow fields surrounding free spinning embryos, pairs and triplets

In the following, we describe a quantitative analysis of the stationary flow fields parallel to the surface (*xy*-plane) as they can be seen around isolated bound embryos, as well as around pairs and triplets rotating near the surface. To this end, we use experimental measurements of tracer particle velocities (see Sec. 1.2 for experimental details) and minimal hydrodynamic arguments to fit the resulting flow fields.

#### 3.2.1 Flow field measurements

*Embryo centroid tracking:* Embryos bound near the surface were segmented using Fiji's [19] built-in function 'Threshold'. Subsequently, incomplete or touching edges of embryos were delineated with the 'Pencil Tool' and the operation 'Fill Holes' was applied. Positions of embryo centroids were then extracted from the resulting shapes using the 'Analyze Particles' feature.

*Tracer particle tracking:* For all measurements, tracer particles were segmented using Fiji's 'Threshold' (i) with and (ii) without applying a prior 'FFT Bandpass Filter' step (filtering structures over 100 pixel  $\approx 200 \mu\text{m}$ ). Segmented particles from (i) and (ii) were then tracked using the 'TrackMate' plugin (Simple LAP tracker) [23]. Combining the results from (i) and (ii) enabled segmentation and tracking of particles with high fidelity both near and far away from the embryo surface.

*Averaging tracer particle velocities:* Before averaging the velocities found from particle tracking, we removed measurements that indicated particle movements away from single embryos or cluster centers by more than  $45^\circ$  to narrow the depth of field. Furthermore, to determine meaningful average flow fields surrounding embryo pairs and triplets, their rotation dynamics had to be taken into account. To this end, the location of a given velocity measurement was additionally registered with respect to the current orientation of the pair or triplet and duplicated with respect to the corresponding cluster symmetry (See Code Availability). Thereby, the final average field corresponds to the instantaneous flow field in the lab frame registered with respect some fixed orientation of the pairs and triplets.

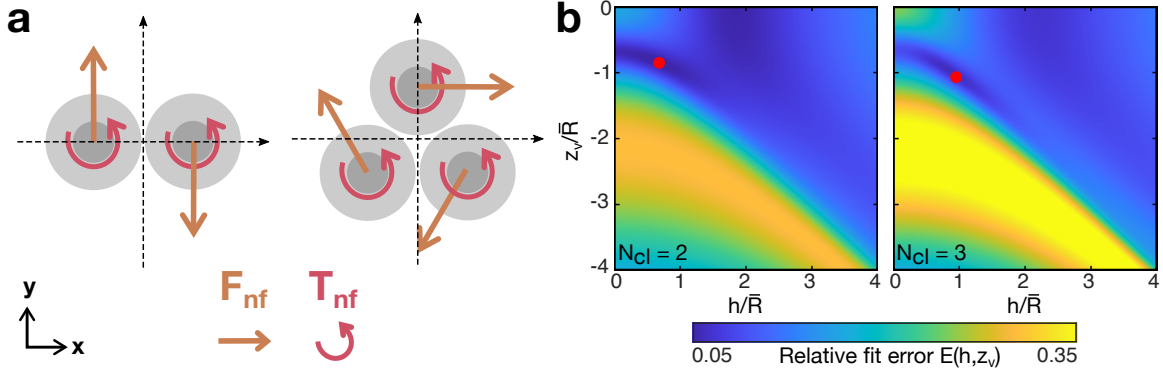


Figure S3: **Fitting of experimental in-plane flow fields.** **a**, Schematic of the locations  $\mathbf{r}_0^{(i)}$  of near-field Stokeslet forces  $\mathbf{F} = F_{nf}\mathbf{e}^{(i)}$  (brown arrows, see Table 2) used to fit flow fields around rotating pairs and triplets. Red arrows indicate corresponding rotlet-associated torques  $\mathbf{T} = T_{nf}\mathbf{e}_z$ . **b**, Relative least squares fit errors  $E(h, z_v) = \langle |\mathbf{u}_{fit} - \mathbf{u}_{exp}| \rangle_{x,y} / \max_{x,y} |\mathbf{u}_{exp}|$  for fits of the  $xy$ -plane flows around the rotating pair (left,  $\bar{R} = 108 \mu\text{m}$ ) and triplet (right,  $\bar{R} = 111 \mu\text{m}$ ) shown in Fig. 2d (main text). Red dots indicate fit parameters that globally minimize  $E(h, z_v)$ .

### 3.2.2 Flow field fitting

To connect average flow fields to the ciliary activity of the embryos, we approximated the flow fields around isolated embryos, pairs and triplets using suitable sets of Stokes flow singularities [6, 5]:

*Single embryos:* The flow surrounding an isolated embryo was approximated by a Stokeslet with strength  $\mathbf{F} = -F_{st}\mathbf{e}_z$  below a free surface [see Eq. (2)] that is centered at the  $(x, y)$ -coordinate of a given embryo centroid and located at a distance  $h$  below the surface. Parameters  $h$ ,  $F_{st}$ , as well as the  $z$ -coordinate  $z_v$  of the apparent  $xy$ -plane in which the flow field is observed, need to be determined from a fit to the flow field measurements (Sec. 3.2.1).

*Additional contributions for rotating pairs and triplets:* Hydrodynamic interactions between the nearby rotating embryo surfaces give rise to an additional exchange of forces and torques that can in turn affect the surrounding flow field [6]. Similar to the Stokeslet Eq. (1), the generic flow around a torque  $\mathbf{T} = (T_x, T_y, T_z)^\top$  located at  $\mathbf{r}_0 = (x_0, y_0, -h)^\top$  in an unbound fluid ('rotlet') is given by

$$\mathbf{u}_{rot}(\mathbf{r}; \mathbf{T}, \mathbf{r}_0) = \frac{1}{8\pi\eta} \frac{\mathbf{T} \times (\mathbf{r} - \mathbf{r}_0)}{|\mathbf{r} - \mathbf{r}_0|^3}. \quad (14)$$

To meet the free-surface boundary conditions at  $\mathbf{r} = (x, y, 0)^\top$  this flow has to be complemented by a rotlet image. The rotlet below a free surface is then given by

$$\bar{\mathbf{u}}_{rot}(\mathbf{r}, \mathbf{T}, \mathbf{r}_0) = \mathbf{u}_{rot}(\mathbf{r}; \mathbf{T}, \mathbf{r}_0) + \mathbf{u}_{rot}(\mathbf{r}; \mathbf{T}', \mathbf{r}'_0), \quad (15)$$

where  $\mathbf{T}' = (-T_x, -T_y, T_z)^\top$  and  $\mathbf{r}'_0 = (x_0, y_0, h)$ .

To fit flow fields around pairs and triplets, we assume each embryo centroid is the source of an 'upright' Stokeslet flow with a common strength  $F_{st}$ . Furthermore, we assume that the exchange of near-field forces is homogeneous and pair-wise symmetric among embryos, such that it can be described by only one additional Stokeslet and rotlet strength,  $F_{nf}$  and  $T_{nf}$ , respectively (Fig. S3a).

*General fit function:* The final flow field that is fitted to measured tracer particle velocity fields

around single embryos ( $N_{cl} = 1$ ), pairs ( $N_{cl} = 2$ ) and triplets ( $N_{cl} = 3$ ) is given by

$$\mathbf{u}_{fit}(\mathbf{r}) = \sum_{i=1}^{N_{cl}} \left[ \bar{\mathbf{u}}_{st} \left( \mathbf{r}; -F_{st}\mathbf{e}_z, \mathbf{r}_0^{(i)} \right) + \bar{\mathbf{u}}_{st} \left( \mathbf{r}; F_{nf}\mathbf{e}^{(i)}, \mathbf{r}_0^{(i)} \right) + \bar{\mathbf{u}}_{rot} \left( \mathbf{r}; T_{nf}\mathbf{e}_z, \mathbf{r}_0^{(i)} \right) \right], \quad (16)$$

where  $\bar{\mathbf{u}}_{st}$  and  $\bar{\mathbf{u}}_{rot}$  are given in Eqs. (2) and (15) and  $F_{nf} = T_{nf} = 0$  for isolated single embryos. For a comparison with measurements, Eq. (16) is evaluated at  $\mathbf{r} = (x, y, z_v)^\top$  and the parameters  $F_{st}, F_{nf}, T_{nf}, h$  and  $z_v$  are determined from a suitable fit procedure (see below). The positions  $\mathbf{r}_0^{(i)}$  of all flow singularities and the orientations  $\mathbf{e}^{(i)}$  of the near-field forces used for these fits are listed in Table 2 and depicted in Fig. S3a.

$N_{cl}$	$\mathbf{r}_0^{(i)}$	$\mathbf{e}^{(i)}$	Fit parameters
1	$-h\mathbf{e}_z$	—	$\{h, z_v, F_{st}\}$
2	$-\frac{l}{2}\mathbf{e}_x - h\mathbf{e}_z$ $\frac{l}{2}\mathbf{e}_x - h\mathbf{e}_z$	$\mathbf{e}_y$ $-\mathbf{e}_y$	$\{h, z_v, F_{st}, F_{nf}, T_{nf}\}$
3	$\frac{l}{2} \left( \mathbf{e}_x - \frac{1}{\sqrt{3}}\mathbf{e}_y \right) - h\mathbf{e}_z$ $-\frac{l}{2} \left( \mathbf{e}_x + \frac{1}{\sqrt{3}}\mathbf{e}_y \right) - h\mathbf{e}_z$ $\frac{l}{\sqrt{3}}\mathbf{e}_y - h\mathbf{e}_z$	$-\frac{1}{2} (\mathbf{e}_x + \sqrt{3}\mathbf{e}_y)$ $\frac{1}{2} (-\mathbf{e}_x + \sqrt{3}\mathbf{e}_y)$ $\mathbf{e}_x$	$\{h, z_v, F_{st}, F_{nf}, T_{nf}\}$

Table 2: Positions  $\mathbf{r}_0^{(i)}$  and near-field force orientations  $\mathbf{e}^{(i)}$  of flow singularities used to fit  $\mathbf{u}_{fit}(\mathbf{r})$  given in Eq. (16) to experimentally measured flow fields.  $l$  denotes average nearest neighbor centroid distances. Fit parameters are given by the distance of the flow singularities to the surface ( $h$ ), the  $z$ -coordinate ( $z_v$ ) of the  $xy$ -plane in which the flow is observed, as well as the strengths  $F_{st}$ ,  $F_{nf}$  and  $T_{nf}$  of the different flow singularities used in  $\mathbf{u}_{fit}(\mathbf{r})$  (Sec. 3.2.2).

*Least squares fit and non-linear optimization:* Fitting parameters that need to be determined are in all cases given by the upright Stokeslet strength  $F_{st}$ , the distance of the flow singularities to the surface  $h$ , and the effective  $z$ -coordinate  $z_v$  of the plane in which the  $xy$ -plane flow is observed. Fits of flow fields surrounding pairs and triplets additionally include a near-field Stokeslet and rotlet strength,  $F_{nf}$  and  $T_{nf}$ , respectively (Fig. S3a). To determine these fitting parameters from flow fields  $\mathbf{u}_{exp}$  measured in the  $xy$ -plane, we proceeded in two steps. First, for a given observation plane  $z_v$  and distance of flow singularities below the surface  $h$ , we note that the fit function  $\mathbf{u}_{fit}$  given in Eq. (16) depends linearly on the Stokes flow parameters  $F_{st}$ ,  $F_{nf}$  and  $T_{nf}$ . Hence, for given  $h$  and  $z_v$ , these singularity strengths can be determined from an exact least squares minimization of the error  $E(h, z_v) = \langle |\mathbf{u}_{fit} - \mathbf{u}_{exp}| \rangle_{x,y} / \max_{x,y} |\mathbf{u}_{exp}|$ , where only the in-plane  $x$ - and  $y$ -components of  $\mathbf{u}_{fit}$  contribute to this error. For pairs and triplets containing embryos of apparent average radius  $\bar{R}$ , the error  $E(h, z_v)$  was determined on a  $100 \times 100$  parameter grid on which  $h/\bar{R}$  and  $z_v/\bar{R}$  are varied in intervals  $[0, 4]$  and  $[-4, 0]$ , respectively, and  $F_{st}$ ,  $F_{nf}$  and  $T_{nf}$  are determined by least squares fitting  $\mathbf{u}_{fit}$  to measured flow fields  $\mathbf{u}_{exp}$  at each point of this  $(h, z_v)$ -parameter grid (Fig. S3b). In a second step, the final fit parameters are chosen from the fit that globally minimizes the error  $E(h, z_v)$  (red dots in Fig. S3b).

*Fit results:* For the flow field around the rotating pair shown in Fig. 2d the fitting procedure described above yields  $F_{st} = 1.1 \text{ nN}$ ,  $F_{nf} = 25.4 \text{ pN}$  and  $T_{nf} = 11 \text{ pN} \cdot \bar{R}$  ( $\bar{R} = 108 \mu\text{m}$ ). For the flow field around the rotating triplet shown in Fig. 2d, we find  $F_{st} = 1.1 \text{ nN}$ ,  $F_{nf} = 19.8 \text{ pN}$  and  $T_{nf} = 23.3 \text{ pN} \cdot \bar{R}$  ( $\bar{R} = 111 \mu\text{m}$ ). Compared to fitting results for single embryos (Fig. S1a, Tab. 1), the Stokeslet strength  $F_{st}$  is reduced, which is most likely due to a lack of flow screening in a pure singularity description of multiple swimmers. Importantly, the signs (=orientations)

of the fitted near-field contributions are consistent with the orientations of forces and torques expected from the hydrodynamic interactions (Fig. 2c (main text), Sec. 2.2): Consistent with  $F_{nf} > 0$  (see Fig. S3a), clockwise spinning of bound embryos indeed leads to a clockwise rotation of pairs and triplets, and consistent with  $T_z = T_{nf} > 0$ , excess torques that arises from the reduced embryo spinning frequencies are expected to point along the positive  $z$ -direction. Furthermore, we note that the ratio of near-field forces and torques from these fits,  $\bar{R}F_{nf}/T_{nf} \approx 2.3$  (pair) and  $\bar{R}F_{nf}/T_{nf} \approx 0.8$  (triplet), are similar to the ratio  $f_0/\tau_0 \approx 0.4$  of near-field force and torque strengths used in the minimal model [Eqs. (11),(13)], where the latter had been determined by matching rotation frequencies of pairs and triplets between theory and experiment (Sec. 2.2.2, Fig. S2c).

### 3.3 Embryo spinning frequencies

*Analysis of embryo spinning frequencies in small clusters:* Average embryo spinning frequencies were determined from the manually measured duration of 10 embryo rotations (data ‘In small clusters’ in Fig. 2f, main text).

*Automated analysis of embryo spinning frequencies in large clusters:* To measure embryo spinning frequencies within clusters containing  $\approx 100$  embryos, we wrote a MATLAB script that measures the angular displacement of each embryo as a function of time. Our approach takes advantage of the inhomogeneous intensity profile within the embryo body that results from the uneven positioning of developing internal organs. We first processed raw videos using Fiji [19] by inverting the pixel intensity and performing a background subtraction. For each embryo, we shifted the origin of the coordinate system to the embryo centroid, and considered pixels within a circular neighborhood with radius equal to the apparent embryo radius. From these pixels, we constructed an angular intensity profile  $I(\theta, t)$  at each time  $t$  by averaging the pixel intensity within sectors of angular width  $\pi/90$ . We then smoothed the angular intensity profile using adjacent averaging of 10 points in  $\theta$  and 500 points in  $t$  to reduce noise and suppress slow global intensity variations, respectively. We then computed the cross-correlation between angular intensity profiles  $I(\theta + \Delta\theta, t + \Delta t)$  and  $I(\theta, t)$  at two time points, and determined the angular lag  $\Delta\theta = \Delta\theta_{max}$  that maximizes this cross-correlation. While the analysis can be performed between successive frames, performing a running average over  $\Delta t$  frames yields a higher signal to noise ratio and hence more accurate results. In practice, we chose  $\Delta t = 3$  frames and subsequently determined the measured dynamics  $\bar{\theta}(t)$  from a cumulative sum over  $\Delta\theta_{max}$ . Finally, we fitted  $\theta(t) = \omega t^2/2$  to the cumulative sum of  $\bar{\theta}(t)$  to determine a noise-robust estimate of the embryo’s spinning frequency  $\omega/(2\pi)$  (data ‘In larger clusters’ in Fig. 2f, main text).

*Analysis of embryo spinning frequencies in the oscillating cluster:* Embryo spinning frequencies inside the oscillating cluster shown in Fig. 4 were not amenable to an automated tracking approach. Therefore, we manually determined the spinning rates of 40 embryos within the cluster and found a value of  $(0.33 \pm 0.13) \text{ min}^{-1}$  (mean  $\pm$  standard deviation,  $n = 40$ ).

### 3.4 Orientational order parameter

To compute the local bond orientational order for each embryo  $i$ , the nearest neighbor embryo is first determined by a delaunay triangulation of embryos within the cluster (using the MATLAB function `delaunay`). A threshold of  $1.5a$  with lattice constant  $a \approx 207 \mu\text{m}$  was applied to exclude cases where nearest neighbors are anomalously determined at the cluster boundary due to irregular cluster shapes. The local bond orientational order parameter [16] is then defined as

$$\psi_6(\mathbf{r}_i) = \frac{1}{N_i} \sum_{j=1}^{N_i} e^{i6\theta_{ij}} \equiv |\psi_6|_i e^{i\phi_i}, \quad (17)$$

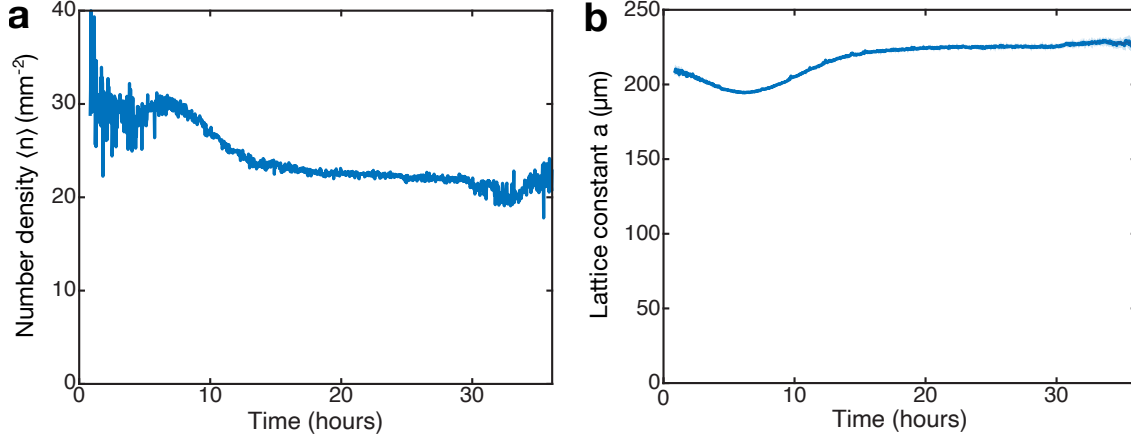


**Figure S4: Time course of average lattice properties.** **a**, Number density  $\langle n \rangle$  of embryos in a crystal over the time course of the experiment. This information was used to compute the radial pair distribution function  $g(r)$  given in Eq. (19) and shown as an inset in Fig. 3f (main text). **b**, Lattice constant as a function of time from fitting the first, nearest-neighbors peak of  $g(r)$ .

where the sum is over the  $N_i$  nearest neighbors of embryo  $i$ , and  $\theta_{ij}$  is the angle of the bond connecting embryo  $i$  and  $j$ , measured with respect to the  $x$ -axis in the frame of the cluster.  $|\psi_6|_i$  quantifies the magnitude of local hexagonal order and  $\phi_i = \arg \psi_6$  measures the angle of the local bond orientational order parameter.

### 3.5 Pair distribution function

Following [4], we define the radial pair distribution function  $g(r)$  as

$$g(r) = \frac{1}{2\pi r N_{cl} \langle n \rangle} \left\langle \sum_{i \neq j} \delta(r - |\mathbf{r}_i - \mathbf{r}_j|) \right\rangle, \quad (18)$$

where  $N_{cl}$  is the total number of centroids in a cluster and  $\langle \cdot \rangle$  denotes the average over all centroids at positions  $\mathbf{r}_i$  and  $\mathbf{r}_j$ . The number density  $\langle n \rangle$  in Eq. (18) was estimated from the rotation-corrected centroid data (see Sec. 3.1) by identifying boundary centroids using the MATLAB function `boundary`, finding the area defined by these boundary centroids using `polyarea`, and dividing the total number of centroids by this area. A time course of the number density  $\langle n \rangle$  is shown in Fig. S4a. The pair distribution  $g(r)$ , e.g. as shown in the inset of Fig 3f (main text), was then computed at 100 s intervals by approximating Eq. (18) at discrete points  $r_k = k\Delta r$  ( $k = 1, 2, 3, \dots$ ) as

$$g(r_k) = \frac{1}{2\pi k N_{cl} \langle n \rangle (\Delta r)^2} \sum_{i \neq j} \mathbb{1}_{r_k \leq |\mathbf{r}_i - \mathbf{r}_j| < r_{k+1}}, \quad (19)$$

which uses an indicator function

$$\mathbb{1}_{r_k \leq |\mathbf{r}_i - \mathbf{r}_j| < r_{k+1}} = \begin{cases} 1 & \text{if } r_k \leq |\mathbf{r}_i - \mathbf{r}_j| < r_{k+1} \\ 0 & \text{else.} \end{cases}. \quad (20)$$

The bin width was  $\Delta r \approx 8.6 \mu\text{m}$ . Finally, the nearest neighbor peak of  $g(r_k)$  was fit to a Gaussian function  $G(r) = C \exp [-(r - \mu)^2 / (2\sigma^2)]$  (Fig. 3f, inset) with fitting parameters describing the amplitude  $C$ , mean  $\mu$ , and width  $\sigma$  of the peak, where  $\sigma$  was taken as the ‘First Peak Width’ plotted in Fig. 3f (main text), and  $\mu$  was taken as the lattice constant  $a$  (Fig. S4b).

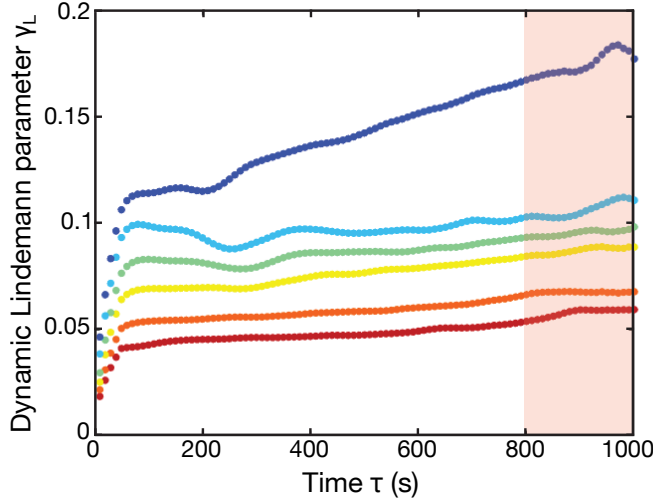


Figure S5: **Dynamic Lindemann parameter.** Representative plots for the dynamic Lindemann parameter  $\gamma_L(\tau)$  (see Sec. 3.6) for developmental times  $t_d$  of 8 h (red), 12 h (orange), 16 h (yellow), 20 h (green), 24 h (light blue) and 28 h (dark blue). The average values and variance of  $\gamma_L(\tau)$  within the shaded region for different developmental times  $t_d$  are shown in Fig. 3g (main text).

### 3.6 Dynamic Lindemann parameter

Following [25] and using rotation-corrected centroid positions (see Sec. 3.1), we define the dynamic Lindemann parameter as

$$\gamma_L(\tau) = \frac{1}{2a^2} \sum_{j,j+1} \left\langle [\Delta\mathbf{r}_j(\tau, t) - \Delta\mathbf{r}_{j+1}(\tau, t)]^2 \right\rangle_t, \quad (21)$$

where  $\Delta\mathbf{r}_i(\tau, t) = \mathbf{r}_i(t + \tau) - \mathbf{r}_i(t)$  denotes the displacement of embryo  $i$  between two time points of duration  $\tau$  apart. Index pairs  $j$  and  $j + 1$  in Eq. (21) correspond to nearest neighbor pairs, and  $a$  is the lattice constant. The analysis takes into account variation of  $a$  with developmental time (Fig. S4b). Two embryos were considered to be nearest neighbors if their initial positions were separated by a distance smaller than  $1.2a$ .

To generate Fig. 3g in the main text, we considered a subset of consecutive developmental time points  $t_d$  that are 100 s apart from each other. The Lindemann parameter  $\gamma_L(\tau)$  is then computed for each  $t_d$  within a centered 1000 s interval, i.e. the average in Eq. (21) was performed over times  $t \in [t_d - 500 \text{ s}, t_d + 500 \text{ s}]$ . Fig. S5 shows representative examples of  $\gamma_L(\tau)$  computed at different developmental time points  $t_d$ . For each  $t_d$ , the mean and standard deviation of  $\gamma_L(\tau)$  over the range  $800 \text{ s} < \tau \leq 1000 \text{ s}$  (20 consecutive time points in total) are plotted as data points and error bars in Fig. 3g (main text), respectively. At very late times beyond 30 h (Fig. 3g in the main text), due to dissolution of the cluster, embryo trajectories do not last over 1000 s, and hence, the dynamic Lindemann parameter cannot be calculated in this regime.

### 3.7 Displacement field and strain components

To determine displacement and strain fields of oscillating clusters (Fig. 4), rotation-corrected centroid trajectories  $\mathbf{r}_i(t)$  (see Sec. 3.1) of embryos  $i = 1, 2, \dots$  were first smoothed with a 5-frame (50 s) moving average to remove noise. We then determined long-time averaged embryo positions  $\mathbf{R}_i(t) = \langle \mathbf{r}_i(t) \rangle_{[t-25, t+25]}$  by using a 50-frame (500 s) moving average. The displacement of each embryo from its average position is given by  $\mathbf{u}(\mathbf{r}_i, t) := \mathbf{u}_i(t) = \mathbf{r}_i(t) - \mathbf{R}_i(t)$  and an exemplary displacement time series is shown in the inset of Fig. 4a (main text). A Fourier-analysis of  $\mathbf{u}(\mathbf{r}_i, t)$  for

all embryos that were continuously tracked throughout a time window of 4000 s revealed an average displacement oscillation frequency of  $(0.26 \pm 0.04) \text{ min}^{-1}$  (mean  $\pm$  standard deviation,  $n = 389$ ). A continuous displacement field  $\mathbf{u}(\mathbf{r}, t)$  was approximated from all embryo displacements  $\mathbf{u}_i(t)$  by applying a 2D Gaussian filter of radius  $a \approx 216 \mu\text{m}$  (approximately one lattice constant). From  $\mathbf{u}(\mathbf{r}, t)$ , we computed the displacement gradient tensor  $u_{\alpha\beta} = \partial u_\alpha / \partial r_\beta$  in the  $xy$ -plane, where  $\alpha, \beta \in \{x, y\}$ . This tensor encodes four principal strain components given by (i) the divergence  $u^0(\mathbf{r}, t) = u_{xx} + u_{yy}$ , (ii) the curl  $u^1(\mathbf{r}, t) = u_{yx} - u_{xy}$ , as well as by the two shear components (iii)  $u^2(\mathbf{r}, t) = u_{xx} - u_{yy}$  ('shear 1'), and (iv)  $u^3(\mathbf{r}, t) = u_{yx} + u_{xy}$  ('shear 2').

To determine space-time kymographs of the strain component dynamics along the boundary shown in Fig. 4d,g (main text), we first determined a parameterization  $\mathbf{r}_s$  of the cluster boundary (MATLAB function `bwboundaries`) in terms of the boundary arc length  $s$ . Finally, components of the displacement gradient tensor  $u_{\alpha\beta}$  were projected onto a local basis composed of the boundary tangent  $\partial_s \mathbf{r}_s$  and the boundary normal pointing away from the cluster to compute transformed strain components  $u^p$  ( $p = 0, 1, 2, 3$ ) analog to the definitions above. This transformation leaves the divergence and curl components  $u^0$  and  $u^1$ , respectively, invariant and corresponds to a rotation of the strain component vector  $(u^2, u^3)^\top$  that conserves the amplitude of the total shear strain  $[(u^2)^2 + (u^3)^2]^{-1/2}$ .

### 3.8 Mode chirality analysis of displacement waves

To characterize the bulk dynamics of cluster oscillations discussed in Fig. 4 (main text) with respect to their chiral symmetry, we consider a complex representation of the displacement field given by

$$U(\mathbf{r}, t) = u_x(\mathbf{r}, t) + i u_y(\mathbf{r}, t). \quad (22)$$

Here,  $i$  denotes the imaginary unit, and  $u_x(\mathbf{r}, t)$  and  $u_y(\mathbf{r}, t)$  represent the Cartesian components of the smoothed, dynamic displacement field  $\mathbf{u}(\mathbf{r}, t)$  described in Sec. 3.7. Using the spatio-temporal Fourier transform of  $U(\mathbf{r}, t)$  given by

$$\tilde{U}(\mathbf{q}, \omega) = \int d\mathbf{r} \int dt U(\mathbf{r}, t) \exp[-i(\mathbf{q} \cdot \mathbf{r} + \omega t)], \quad (23)$$

a mode chirality parameter can be defined as

$$A(\omega) = \frac{\langle |\tilde{U}(\mathbf{q}, \omega)| - |\tilde{U}(-\mathbf{q}, -\omega)| \rangle_{\text{BZ}}}{\langle |\tilde{U}(\mathbf{q}, \omega)| + |\tilde{U}(-\mathbf{q}, -\omega)| \rangle_{\text{BZ}}}. \quad (24)$$

Averages  $\langle \cdot \rangle_{\text{BZ}}$  over wave vectors  $\mathbf{q}$  are taken within the first Brillouin zone defined by the lattice constant  $a \approx 220 \mu\text{m}$  of the hexagonal embryo cluster. The quantity  $|A(\omega)|$  characterizes the symmetry of the displacement field's Fourier spectrum  $\tilde{U}(\mathbf{q}, \omega)$  with respect to point-reflections at the Fourier space origin and therefore corresponds to a measure of broken PT-symmetry. It vanishes if the spectrum is perfectly point-symmetric and becomes unity if the PT-symmetry of a given mode is maximally broken. In practice,  $A(\omega)$  given in Eq. (24) can be used to detect and quantify signatures of chirality in oscillating displacement fields. To see this explicitly, it is instructive to consider a minimal displacement wave of the form

$$u_x(\mathbf{r}, t) = u_x^{(0)} \cos(\Omega t - \lambda x) \quad (25a)$$

$$u_y(\mathbf{r}, t) = u_y^{(0)} \sin(\Omega t - \lambda x), \quad (25b)$$

for some frequency  $\Omega$  and wavelength  $\lambda$ . The wave described by Eqs. (25) represents a pure longitudinal (transverse) wave if  $u_x^{(0)} \neq 0$  and  $u_y^{(0)} = 0$  ( $u_x^{(0)} = 0$  and  $u_y^{(0)} \neq 0$ ). In either case, the Fourier amplitude of the complex representation Eq. (22) is point-symmetric, i.e.  $|\tilde{U}(\mathbf{q}, \omega)| = |\tilde{U}(-\mathbf{q}, -\omega)|$  and consequently  $A(\omega) = 0$  [see Eq. (24)] for purely longitudinal or transverse waves.

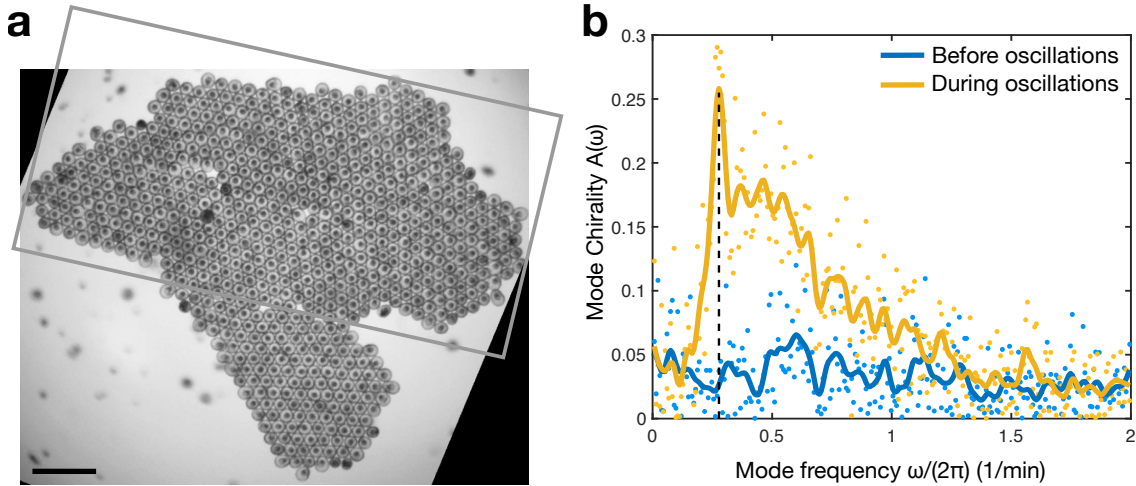


**Figure S6: Mode chirality analysis of displacement waves.** **a,** The mode chirality analysis described in Sec. 3.8 was performed on a  $7.8 \times 3.9$  mm region of interest indicated by the gray box over a time window of 135 min. Scale bar, 1 mm **b,** Mode chirality parameter  $A(\omega)$  given in Eq. (24) before the onset of (blue dots) and during (yellow dots) visible oscillations. A smoothed representation of this mode data is depicted by solid lines and serves as guide to the eye. Black dashed line indicates most prominent chiral oscillations at a frequency of approximately  $0.28 \text{ min}^{-1}$ .

However, if both amplitudes of the minimal wave in Eq. (25) are finite,  $u_x^{(0)} \neq 0$  and  $u_y^{(0)} \neq 0$ , the wave acquires a chiral character, as seen by the well-defined rotation sense of displacement vectors at every point  $\mathbf{r}$ . In this case, the point-symmetry in Fourier-space is lost and  $|A(\omega = \Omega)| \neq 0$ . Interestingly, for  $u_x^{(0)} = u_y^{(0)}$  the displacement vector Eq. (25) draws out perfect circles at every point  $\mathbf{r}$ , a characteristic of emergent displacement waves that can appear in purely odd elastic materials [18]. In this case, the chirality measure defined in Eq. (24) becomes maximal at the wave frequency, i.e.  $|A(\omega = \Omega)| = 1$ .

We have determined  $A(\omega)$  from displacement field information  $\mathbf{u}(\mathbf{r}, t)$  located in the domain shown in Fig. S6a (gray box,  $900 \times 450$  pixel, corresponding to  $7.8 \times 3.9$  mm). Points of this domain outside the cluster were zero-padded. We then considered temporal sections of 800 consecutive time points ( $\approx 135$  min in total) before the onset of and during cluster oscillations. For each section, we computed a fast Fourier transform (MATLAB function `fftn` [9]) of the resulting  $900 \times 450 \times 800$  data-cubes to approximate the Fourier transform Eq. (23) and determine  $A(\omega)$  given in Eq. (24). During oscillations, a broad spectrum of frequencies shows chiral signatures (yellow curve in Fig. S6b), including a distinct peak with frequency  $\approx 0.28 \text{ min}^{-1}$  (black dashed line). An almost identical frequency ( $0.26 \text{ min}^{-1}$ ) is found from a direct analysis of the space-time kymographs that characterize strain component oscillation along the cluster boundary (see Fig. 4d,g (main text) and Sec. 3.7). In the absence of visible cluster oscillations  $|A(\omega)|$  flattens substantially (blue curve in Fig. S6b).

### 3.9 Phase space current and partial entropy production

The entropy production rate  $\dot{S}$  of an overdamped stochastic system that follows Langevin dynamics can be determined from [15]

$$\dot{S} = k_B \int d\mathbf{x} \frac{\mathbf{j}(\mathbf{x}) \cdot \mathbf{D}^{-1}(\mathbf{x}) \cdot \mathbf{j}(\mathbf{x})}{\rho(\mathbf{x})}, \quad (26)$$

where  $\rho(\mathbf{x})$  and  $\mathbf{j}(\mathbf{x})$  denote the probability density and corresponding probability current of a particular system configuration  $\mathbf{x}$ , respectively.  $\mathbf{D}(\mathbf{x})$  is an effective diffusion matrix with inverse  $\mathbf{D}^{-1}(\mathbf{x})$ . In the following, we describe how  $\rho$ ,  $\mathbf{j}$  and  $\mathbf{D}$  can be approximated from experimental data of the strain component dynamics to estimate the system's partial entropy production rate shown in Fig. 4e,f,h,i (main text) using Eq. (26).

For the spatially resolved analysis shown in Fig. 4e,h, we tiled the cluster domain into square regions of  $200\ \mu\text{m}$  (approximately one embryo diameter). The center of each tile is located at some position  $\hat{\mathbf{r}}$ . In each of these squares, we spatially average the strain components  $u^p(\mathbf{r}, t)$  ( $p = 0, 1, 2, 3$ , see Sec. 3.7) to determine local strain component values  $\hat{u}^p(\hat{\mathbf{r}}, t)$ . We then introduce a strain component pair vector  $\hat{\mathbf{u}}(\hat{\mathbf{r}}, t) = [\hat{u}^p(\hat{\mathbf{r}}, t), \hat{u}^q(\hat{\mathbf{r}}, t)]^\top$ . Inspired by the divergence-curl and shear 1-shear 2 cycles that were suggested as signatures of odd elastic oscillations [18], we considered for our analysis the corresponding pairs  $p = 0, q = 1$  (Fig. 4e,f in the main text) and  $p = 2, q = 3$  (Fig. 4h,i in the main text).

To estimate partial entropy production rates, we used time series of strain component pairs  $\{\hat{\mathbf{u}}_1, \hat{\mathbf{u}}_2, \dots, \hat{\mathbf{u}}_N\}$ , where  $\hat{\mathbf{u}}_k := \hat{\mathbf{u}}(\hat{\mathbf{r}}, k\Delta t)$  with  $k = 1, 2, \dots, N$  denotes pairs of strain components at  $N = 200$  successive time points in  $\Delta t = 10\ \text{s}$  intervals. The continuous probability density  $\rho(\mathbf{x})$  and the associated current  $\mathbf{j}(\mathbf{x})$  were then estimated as [11]:

$$\hat{\rho}(\mathbf{x}) = \frac{1}{N} \sum_{i=1}^N K(\mathbf{x}, \hat{\mathbf{u}}_i, \Sigma), \quad (27a)$$

$$\hat{\mathbf{j}}(\mathbf{x}) = \frac{\hat{\rho}(\mathbf{x})}{2\Delta t} \frac{\sum_{i=2}^{N-1} K(\mathbf{x}, \hat{\mathbf{u}}_i, \Sigma)(\hat{\mathbf{u}}_{i+1} - \hat{\mathbf{u}}_{i-1})}{\sum_{i=2}^{N-1} K(\mathbf{x}, \hat{\mathbf{u}}_i, \Sigma)}, \quad (27b)$$

where system configurations  $\mathbf{x} = (u^p, u^q)^\top$  are defined in the space of a strain component pair. In Eqs. (27),  $K(\mathbf{x}, \boldsymbol{\mu}, \Sigma) = \exp[-(\mathbf{x} - \boldsymbol{\mu})^\top \Sigma^{-1}(\mathbf{x} - \boldsymbol{\mu})/2]/[2\pi \det(\Sigma)]^{-1/2}$  is the bivariate Gaussian with a bandwidth  $\Sigma$  determined using the ‘rule of thumb’ [3, 15]. Examples of the probability densities and fluxes estimated at some position in the cluster using Eqs. (27) are shown in the insets of Fig. 4e,h (main text). Similarly, the effective diffusion matrix is estimated as [11]

$$\bar{\mathbf{D}}(\mathbf{x}) = \frac{\hat{\rho}(\mathbf{x})}{\Delta t} \frac{\sum_{i=1}^{N-1} K(\mathbf{x}, \hat{\mathbf{u}}_i, \Sigma)(\hat{\mathbf{u}}_{i+1} - \hat{\mathbf{u}}_i) \otimes (\hat{\mathbf{u}}_{i+1} - \hat{\mathbf{u}}_i)}{\sum_{i=1}^{N-1} K(\mathbf{x}, \hat{\mathbf{u}}_i, \Sigma)}, \quad (28)$$

where  $\otimes$  denotes a dyadic product. To ensure an inverse diffusion matrix required in Eq. (26) is well-defined, we finally use  $\bar{\mathbf{D}}(\mathbf{x})$  given in Eq. (28) to define a constant, weighted mean diffusion matrix  $\hat{\mathbf{D}}$  as

$$\hat{\mathbf{D}} = \int d\mathbf{x} \bar{\mathbf{D}}(\mathbf{x}) \hat{\rho}(\mathbf{x}) \mathbb{1}_{\hat{\rho}(\mathbf{x}) > c}. \quad (29)$$

Here,  $\mathbb{1}_{\hat{\rho}(\mathbf{x}) > c}$  is the indicator function defined analog to Eq. (20) and  $c$  is chosen such that only sufficiently well populated regions of the phase space with  $\hat{\rho}d\mathbf{x} > 0.01$  are included in the analysis. The estimates Eqs. (27) and Eq. (29) are then used in Eq. (26) to approximate a local partial entropy production rate  $\hat{S}(\hat{\mathbf{r}})$ . Finally, the spatially integrated entropy production rate for the whole cluster (Fig. 4f,i in the main text) is given by

$$\hat{S}_{\text{tot}} = \sum_{\hat{\mathbf{r}}} \hat{S}(\hat{\mathbf{r}}). \quad (30)$$

To test the robustness of the spatially integrated entropy production rate, we performed the same analysis on bootstrapped [8, 1] time series of the strain component pairs. In particular, we randomly sampled  $N - 2$  elements from the time series of strain component pair vectors  $\{\hat{\mathbf{u}}_2, \hat{\mathbf{u}}_3, \dots, \hat{\mathbf{u}}_{N-1}\}$ . With each sampled vector  $\hat{\mathbf{u}}_k$ , we additionally stored  $\hat{\mathbf{u}}_{k-1}$  and  $\hat{\mathbf{u}}_{k+1}$  to be able to compute the flux and diffusion matrix given in Eqs. (27b) and (29). Entropy production rates were finally determined from this bootstrapped configuration space information. Repeating this procedure 100 times yields a standard deviation that is depicted by error bars in Fig. 4f,i.

## References

- [1] C. Battle, C. P. Broedersz, N. Fakhri, V. F. Geyer, J. Howard, C. F. Schmidt, and F. C. MacKintosh. Broken detailed balance at mesoscopic scales in active biological systems. *Science*, 352(6285):604–607, 2016.
- [2] D. Blair and E. Dufresne. Matlab particle tracking.
- [3] A. W. Bowman and A. Azzalini. *Applied smoothing techniques for data analysis: the kernel approach with S-Plus illustrations*, volume 18. OUP Oxford, 1997.
- [4] P. M. Chaikin and T. C. Lubensky. *Principles of Condensed Matter Physics*. Cambridge University Press, 1995.
- [5] K. Drescher, R. E. Goldstein, N. Michel, M. Polin, and I. Tuval. Direct measurement of the flow field around swimming microorganisms. *Phys. Rev. Lett.*, 105:168101, 2010.
- [6] K. Drescher, K. C. Leptos, I. Tuval, T. Ishikawa, T. J. Pedley, and R. E. Goldstein. Dancing Volvox: Hydrodynamic Bound States of Swimming Algae. *Phys. Rev. Lett.*, 102:168101, 2009.
- [7] E. R. Dufresne, T. M. Squires, M. P. Brenner, and D. G. Grier. Hydrodynamic coupling of two brownian spheres to a planar surface. *Phys. Rev. Lett.*, 85:3317–3320, 2000.
- [8] B. Efron. Bootstrap Methods: Another Look at the Jackknife. *Ann. Stat.*, 7(1):1 – 26, 1979.
- [9] M. Frigo and S. G. Johnson. Fftw: an adaptive software architecture for the fft. In *Proceedings of the 1998 IEEE International Conference on Acoustics, Speech and Signal Processing, ICASSP '98 (Cat. No.98CH36181)*, volume 3, pages 1381–1384, 1998.
- [10] H. Ishii, T. Shirai, C. Makino, and T. Nishikata. Mitochondrial inhibitor sodium azide inhibits the reorganization of mitochondria-rich cytoplasm and the establishment of the anteroposterior axis in ascidian embryo. *Dev. Growth Differ.*, 56(2):175–188, 2014.
- [11] W. Just, H. Kantz, M. Ragwitz, and F. Schmüser. Nonequilibrium physics meets time series analysis: Measuring probability currents from data. *EPL*, 62(1):28, 2003.
- [12] S. Kim and S. J. Karrila. *Microhydrodynamics: Principles and Selected Applications*. Dover Civil and Mechanical Engineering. Dover Publications, 2013.
- [13] H. W. Kuhn. The Hungarian method for the assignment problem. *Nav. Res. Logist.*, 2(1):83–97, 1955.
- [14] E. Lauga. *The Fluid Dynamics of Cell Motility*. Cambridge Texts in Applied Mathematics. Cambridge University Press, 2020.
- [15] J. Li, J. M. Horowitz, T. R. Gingrich, and N. Fakhri. Quantifying dissipation using fluctuating currents. *Nat. Comm.*, 10(1):1–9, 2019.
- [16] D. R. Nelson and B. Halperin. Dislocation-mediated melting in two dimensions. *Phys. Rev. B*, 19(5):2457, 1979.
- [17] A. P. Petroff, X.-L. Wu, and A. Libchaber. Fast-moving bacteria self-organize into active two-dimensional crystals of rotating cells. *Phys. Rev. Lett.*, 114:158102, 2015.
- [18] C. Scheibner, A. Souslov, D. Banerjee, P. Surówka, W. T. M. Irvine, and V. Vitelli. Odd elasticity. *Nat. Phys.*, 16(4):475–480, 2020.

- [19] J. Schindelin, I. Arganda-Carreras, E. Frise, V. Kaynig, M. Longair, T. Pietzsch, S. Preibisch, C. Rueden, S. Saalfeld, B. Schmid, et al. Fiji: an open-source platform for biological-image analysis. *Nat. Methods*, 9(7):676–682, 2012.
- [20] Z. Shen, A. Würger, and J. S. Lintuvuori. Hydrodynamic self-assembly of active colloids: chiral spinners and dynamic crystals. *Soft Matter*, 15:1508–1521, 2019.
- [21] S. E. Spagnolie and E. Lauga. Hydrodynamics of self-propulsion near a boundary: predictions and accuracy of far-field approximations. *J. Fluid Mech.*, 700:105–147, 2012.
- [22] T. M. Squires. Effective pseudo-potentials of hydrodynamic origin. *J. Fluid Mech.*, 443:403–412, 2001.
- [23] J.-Y. Tinevez, N. Perry, J. Schindelin, G. M. Hoopes, G. D. Reynolds, E. Laplantine, S. Y. Bednarek, S. L. Shorte, and K. W. Eliceiri. Trackmate: An open and extensible platform for single-particle tracking. *Methods*, 115:80–90, 2017.
- [24] W. Yan, E. Corona, D. Malhotra, S. Veerapaneni, and M. Shelley. A scalable computational platform for particulate stokes suspensions. *J. Comp. Phys.*, 416:109524, 2020.
- [25] K. Zahn, R. Lenke, and G. Maret. Two-stage melting of paramagnetic colloidal crystals in two dimensions. *Phys. Rev. Lett.*, 82:2721–2724, 1999.